International Journal of Machine Tools & Manufacture 171 (2021) 103805

Contents lists available at ScienceDirect

International Journal of Machine Tools and Manufacture

journal homepage: www.elsevier.com/locate/ijmactool

Rapid stability analysis of serrated end mills using graphical-frequency domain methods

Pritam Bari [a], Zekai Murat Kilic [b,*], Mohit Law [a], Pankaj Wahi [a]

[a] Machine Tool Dynamics Laboratory, Department of Mechanical Engineering, Indian Institute of Technology Kanpur, Uttar Pradesh, 208016, India
[b] Department of Mechanical, Aerospace and Civil Engineering, The University of Manchester, Manchester, M13 9PL, United Kingdom

ARTICLE INFO

Keywords:
Serrated end mills
Varying time delays
Chatter stability
Graphical
Frequency domain

ABSTRACT

Serrated tools result in an irregular distribution of chip thickness and varying time delays along their flutes that disturb the regenerative chatter mechanism and maximize productivity in rough machining operations. The chatter stability simulation with such tools is complex due to the delay differential equations with multiple and distributed delays. Although the time domain numerical integration methods and the semi-discretization method are accurate, they are computationally expensive and hence inhibit the optimal design of serrated cutters. Despite the advantages that serrated tools offer, there has been little attention paid to rapidly predict stability lobes diagram for these tools to help instruct their optimal designs. To address this need, new graphical-frequency methods are presented to solve for stability of serrated tools with arbitrary geometry. The graphical method averages the number of teeth in cut to make the system time-invariant and results in a closed-form analytical solution. It reduces the simulation time by up to ~99% compared to the semi-discretization method. Generalized solutions to the classical zero-order approximation and the multi-frequency methods are also presented by using the Nyquist stability criterion. The use of the zero-order approximation method and the multi-frequency method reduces simulation times by up to ~97% and ~79% respectively compared to the semi-discretization method. These are significant improvements over reports in the previous literature. Stability predictions are validated experimentally and benchmarked with high-fidelity time domain methods. The presented methods are general and can be applied to any end mill with non-uniform pitch and helix angles as well.

1. Introduction

Serrated end mills enable high-performance chatter-free rough machining. Their cutting performance is governed by the geometry of the serration profile, by the phase shift between the profiles on different teeth [1,2], and by the ratio of the feed per tooth to the amplitude of the serration profile [3,4]. Well-designed serration geometry and preferential phase-shifts between the profiles on different teeth along with low ratios of the feed per tooth to the amplitude of the serration profile result in irregular chip thickness distributions, in the total depth of cut being less than the apparent depth of cut due to the missed-cut effect, and in varying time delays [2,4]. These effects are combined to disturb the regenerative mechanism responsible for chatter [2,4], making high-performance chatter-free rough machining possible. Furthermore, at low ratios of the feed per tooth to the amplitude of the serration profile, the ratio of the apparent depth of cut to the actual depth of cut is also low. As a result, serrated end mills cut thicker chips at the regions where cutting occurs, and a reduction in average cutting forces, torque and power requirements is achieved due to the size effect [4]. Though these cutters are beneficial, their manufacture involves a significant additional cost to grind serration profiles atop regular end mills [5]. Hence a stability model is essential to guide design and manufacture of such tools.

Serrated cutters can take many forms including non-uniform helix and pitch angles [6–10], with many ways to further define the waveform geometry and phase shifts [2,9,11]. Even though serrated cutters with non-uniform helix and pitch may not significantly influence stability [4], such cutters exist [9]. Since there is a high number of input parameters influencing the performance of serrated cutters, a generalized stability model that can predict performance rapidly and accurately will enable smart design and manufacturing process of these cutters in industrial settings. The main aim of this paper is to present such stability models for serrated end mills.

Machining stability models, in general, are based on the dynamics of the system, the cutting force characteristic, and the tool-workpiece

* Corresponding author.
E-mail address: zekaimurat.kilic@manchester.ac.uk (Z.M. Kilic).

https://doi.org/10.1016/j.ijmachtools.2021.103805
Received 26 June 2021; Received in revised form 20 September 2021; Accepted 22 September 2021
Available online 28 September 2021

Nomenclature

a_p	Axial depth of cut
$a_{p_{lim}}$	Limiting axial depth of cut at the stability boundary
a_1, a_2, a_3	Length of three zones in the grey portion of the chip thickness cross-section
A	Amplitude of the serration profile
$\mathbf{A}_i(z,t)$	Time-varying elemental directional dynamic milling force coefficient matrix for the i^{th} flute at height z and time t
$\mathbf{A}_i^0(z)$	Mean dynamic force coefficient matrix for the i^{th} flute at height z
$b_i^0(\omega,z)$	Regenerative coefficient for the i^{th} flute at height z
$\mathbf{C}$	Modal damping matrix
dz	Length of axial discretized element of the serrated cutter
$d\mathbf{F}^{dc}{}_{xy,i}(z,t)$	Elemental dynamic forces in the x-y plane for the i^{th} flute at the height z at time t
$d\mathbf{F}^{dc}{}_{rta,i}(z,t)$	Elemental dynamic forces in the *rta* frame for the i^{th} flute at the height z at time t
D	Diameter of the serrated cutter
$f_{i,l}(z,t)$	Feed per revolution between the i^{th} and $(i+l)^{th}$ flute at the height z at time t
f_t	Feed per tooth per revolution
f_x, f_y	Modal frequency (Hz) in x and y directions
F	Amplitude of the resulting cutting force $F_{res}(t)$
$F_n(t)$	Non-regenerative force at the time t
$F_r(t)$	Regenerative force at the time t
$F_{res}(t)$	Resultant force at the time t
$\mathbf{F}_{xy}^{dc}(t)$	Lumped dynamic cutting force vector in the x-y plane
$\mathbf{F}_{xy}^{st}(t)$	Lumped static cutting force vector in the x-y plane
$g_i(z,t)$	Screening function for the i^{th} flute at the height z at time t
$h_i^{dc}(z,t)$	Elemental dynamic chip thickness for the i^{th} flute at the height z at time t
$h_i^{st}(z,t)$	Elemental static chip thickness for the i^{th} flute at the height z at time t
$\mathbf{H}(j\omega)$	FRF matrix with direct and cross transfer functions
$H_{or}(j\omega)$	Oriented FRF
i	Flute index for any flute of the N-fluted cutter
k_r	Modal stiffness for the r^{th} mode
k_x, k_y	Modal stiffness in x and y directions
$\mathbf{K}$	Modal stiffness matrix
$\mathbf{K}^c$	Primary cutting force coefficient vector
K_s	Resultant cutting force coefficient
K_t^c, K_r^c, K_a^c	Primary cutting force coefficients along tangential, radial, and axial directions of the *rta* frame
l	Dummy index
L	Number of axial infinitesimal elements along chip thickness cross-section
m	Total number of modes
m_x	m_y Number of modes in x and y directions
M	Stability metric in the time-domain Euler integration method
$\mathbf{M}^{-1}$	Inverse of the modal mass matrix
n	Spindle speed (rpm)
$\vec{\mathbf{n}}$	Average chip thickness direction
N	Number of flutes (teeth) of the serrated cutter
N_t	Effective number of flutes
$\mathbf{q}(t)$	Modal displacement vector
r	Subscript for mode number
$R_i(z)$	Local radius of the serrated cutter for the i^{th} flute at the height z
t	Time
T	Spindle rotation period
T_s	Tooth-passing period
$\mathbf{T}_{xr,i}(z,t)$	Force transformation matrix from *rta* to *xyz* coordinate for the i^{th} flute at height z at time t
$u(t)$	Tool displacement response along the average chip thickness direction $\vec{\mathbf{n}}$
$\mathbf{U}$	Mode shape matrix
$x(t)$	Current vibration in x direction
$x(t-\tau_i(z,t))$	Past vibration in x direction
$y(t)$	Current vibration in y direction
$y(t-\tau_i(z,t))$	Past vibration in y direction
z	Axial location along the flute
α_j	Screening function along chip cross section
β	Angle between the non-regenerative force $F_n(t)$ and resultant force $F_{res}(t)$
β_r	Angle between average chip thickness direction $\vec{\mathbf{n}}$and resultant force $F_{res}(t)$
ζ_r	Modal damping ratio for the r^{th} mode
ζ_x, ζ_y	Modal damping ratio in x and y directions
$\eta_i(z)$	Local helix angle for the i^{th} flute at height z
$\kappa_i(z)$	Axial immersion angle for the i^{th} flute at height z
λ	Wavelength of the serration profile
$\nu_i(z,t)$	Number of flutes skipped due to the missed-cut
$\tau_i(z,t)$	Time delay at height z and time t between the current vibration made by the i^{th} flute and the past vibration made by the $(i+l)^{th}$ flute
ϕ	Phase lag between the resultant cutting force $F_{res}(t)$ and tool displacement response $u(t)$
φ_{ex}	Exit radial immersion angle
$\varphi_i(z,t)$	Radial immersion angle for i^{th} flute at height z and time t
$\varphi_{p,i}(z)$	Local pitch angle between $i^{th}$and $(i+1)^{th}$ flute at height z
φ_{st}	Entry radial immersion angle
$\mathbf{\Phi}$	Transition matrix over the principal period T
ψ_i	Initial phase shift for the i^{th} flute at the starting of the serration profile
ω	Vibration frequency (rad/sec)
ω_c	Chatter frequency (rad/sec)
ω_r	Modal frequency (rad/sec) for the mode
Ω	Spindle rotational speed (rad/sec)
FRF	Frequency response function
MFS	Multi-frequency solution
rta	Rotating radial-tangential-axial frame
SDM	Semi-discretization method
xyz	Non-rotating body-fixed coordinate system
ZOA	Zero-order approximation method

engagement conditions. These models are described by delay differential equations that characterize the regeneration phenomena in which the response of the current state depends on the previous state(s). Since phase shifts of the serration profile from one tooth to the next result in an irregular distribution of the chip thickness [2,4], and since there can be instances of the missed-cut effect in which the dynamic chip thickness depends on not only the previous tooth, but on the cutting action of several teeth that may have passed previously [4], and since there can also be the case of self-interruption due to large amplitude vibrations resulting in loss of contact between the tool and the workpiece [12], the multiple delays for serrated end mills are continuously distributed. This is unlike regular end mills in which the single delay is constant.

Characterizing stability behavior for tools with multiple delays, though non-trivial, is easier still using time-domain numerical methods

than frequency domain methods. Thus, almost all previous research concerned with stability analysis for serrated end mills has used time-domain numerical methods to solve for their stability [2,4,7,13–19]. These time-domain methods have been based on the standard forward Euler numerical integration scheme [13,14] and on the established and computationally more efficient semi-discretization method [20] and full-discretization method [21]. In the methods using numerical integration, response at the operating point is monitored to check if the system is stable or not, whereas, in the semi-discretization method, the eigenvalues of the periodic state transition matrix are probed to check for stability at the operating point of interest. Though these time-domain methods provide a local picture about a particular operating point being stable or not, establishing stability boundaries requires different depths of cut to be scanned at every spindle speed in the range of interest. The methods are hence time consuming and can sometimes take many hours to predict stability boundaries for serrated end mills.

Though stability analysis in the frequency domain, especially with the use of classical zero-order approximation (ZOA) method [22] is computationally more efficient than time domain methods, the method is approximate and handling multiple delays in the frequency domain is not trivial. The ZOA method gives analytical solutions to the case with single, constant delay [22], and hence it is not suitable for serrated end mills unless the delay is averaged across the helical flute and across different teeth – as was done in Ref. [23]. Contemporary work [24] discretized the serrated end mill into cylindrical elements along its axis and used the ZOA method by averaging the time-varying delay and the time-varying directional factors in every element. The ZOA method has also been used to analyze stability for systems with multiple delays, such as in the case of stability of tools with variable helix and/or pitch [25–29].

Since the ZOA method averages the periodic components of the cutting force characteristic by the average of the Fourier harmonics, the method suffers from accuracy issues for low immersion milling, and for intermittent cutting that is a characteristic of serrated end milling. To address this shortcoming, the multi-frequency solution (MFS) suggested including higher harmonics of the periodic solution [30]. However, that method too was originally applicable to systems with a single and constant delay. Hence, the MFS method was subsequently extended to incorporate the influence of distributed delays for complex tools [31,32]. Though the extended MFS method can handle distributed delays, the method required the use of a multi-dimensional bisection method to find roots, resulting in slow computation due to the iterative eigenvalue calculations.

Another class of frequency domain models for stability that are computationally very efficient are the so-called graphical methods [33]. These methods are like the Tlusty's average tooth angle approach [13] which presents an analytical stability solution by averaging the time-varying cutting forces and assuming an average direction of chip thickness and an average force direction with an average number of teeth in cut. The graphical methods were cleverly extended by Stone [5] to include the influence of multiple delays for the case of serrated end mills. However, the methods presented by Stone [5] were limited to only two types of serration waveforms with fixed number of teeth and were not generalized to handle different serration profiles with any number of teeth and for cutters with non-uniform pitch and helix angles.

Though graphical methods are approximate, they facilitate rapid analysis of stability due to their geometrical implementations. And, as this research will show, characterizing stability boundaries for serrated end mills with these methods takes only a few seconds. This paper proposes, for the first time, generalized graphical methods to solve for stability of serrated end mills. The proposed methods will be shown to be capable of handling serrated cutters with arbitrary geometry along with being capable of handling complex profiled serrated cutters with non-uniform pitch and helix.

In addition to presenting a generalized graphical method for rapid stability analysis for serrated cutters, this paper will also generalize solutions to the ZOA and the MFS methods using the Nyquist stability criterion, which has been used to solve for stability of turning and milling systems [34–36]. Though an approximated ZOA method was earlier proposed in Ref. [23], where the dynamic forces were averaged out to solve stability for serrated cutter, that approach followed a computationally costly iterative search method unlike we do with the use of the Nyquist stability criterion in our paper. And even though contemporary work [24] also averaged the delay and solved the resulting characteristic equation using the Nyquist stability criterion, their averaging led to deviations from experiments and from predictions using time-domain methods. Also, our MFS solution does not require the additional step of using a root finding technique as was suggested in Ref. [31]. As such, these frequency domain methods, as will be shown herein, are accurate and computationally efficient. Using the Nyquist criterion to solve for the generalized stability of serrated end mills in the frequency domain is another contribution of the current research. To contextualize the efficacy of our proposed methods of stability analysis, model predictions will be compared with established time-domain solution methods.

The remainder of the paper is structured as follows. At first, Section 2 describes established models of the dynamic chip thickness, the cutting force, and the dynamical governing equations of motion. Section 3 presents methods to solve for stability. The graphical methods therein are illustrated for three different serrated cutters, one non-standard profiled cutter with uniform helix and teeth spacing, another standard profiled serrated cutter with uniform helix and teeth spacing, and a non-standard profiled cutter with non-uniform pitch and helix. Section 3 also describes methods to solve for stability using the Nyquist stability criterion with the frequency domain methods as well as briefly overviews solution methods in the time domain. Section 4 experimentally validates model prediction. Section 5 discusses the limitation of our stability models. This is followed by the main conclusions in Section 6.

2. Cutting mechanics and dynamics of serrated end mills

Cutting mechanics and dynamics of serrated end mills are already well established [2,4,9,16]. To contextualize what makes solving for machining stability of these special cutters different than regular ones, we briefly outline the dynamic chip thickness model, the cutting force model, and the governing equations of motion that are to be solved to characterize stability. The models described in brief herein are based on detailed reports in Refs. [2,4,9,16].

Assuming the tool to be flexible in the x and y directions, the cutting forces excite it in the feed (x), and feed normal (y) directions causing dynamic displacements as shown in Fig. 1.

Since the tool's geometry is complex, we analyze forces in elements discretized along the tool's axis. In each element, we attach a radial-tangential-axial (*rta*) frame to evaluate elemental dynamic forces that are then transformed to a fixed *xyz* frame as follows:

$$\mathrm{d}\mathbf{F}^{\mathrm{dc}}_{xy,i}(z,t) = \mathbf{T}_{xr,i}(z,t)\left[\mathrm{d}F^{\mathrm{dc}}_{r,i}(z,t)\ \mathrm{d}F^{\mathrm{dc}}_{t,i}(z,t)\ \mathrm{d}F^{\mathrm{dc}}_{a,i}(z,t)\right]^{\mathrm{T}} = \mathbf{T}_{xr,i}(z,t)\left[\mathbf{K}^{\mathrm{c}}\ h^{\mathrm{dc}}_{i}(z,t)\right]\frac{\mathrm{d}z}{\sin\kappa_i(z)}, \tag{1}$$

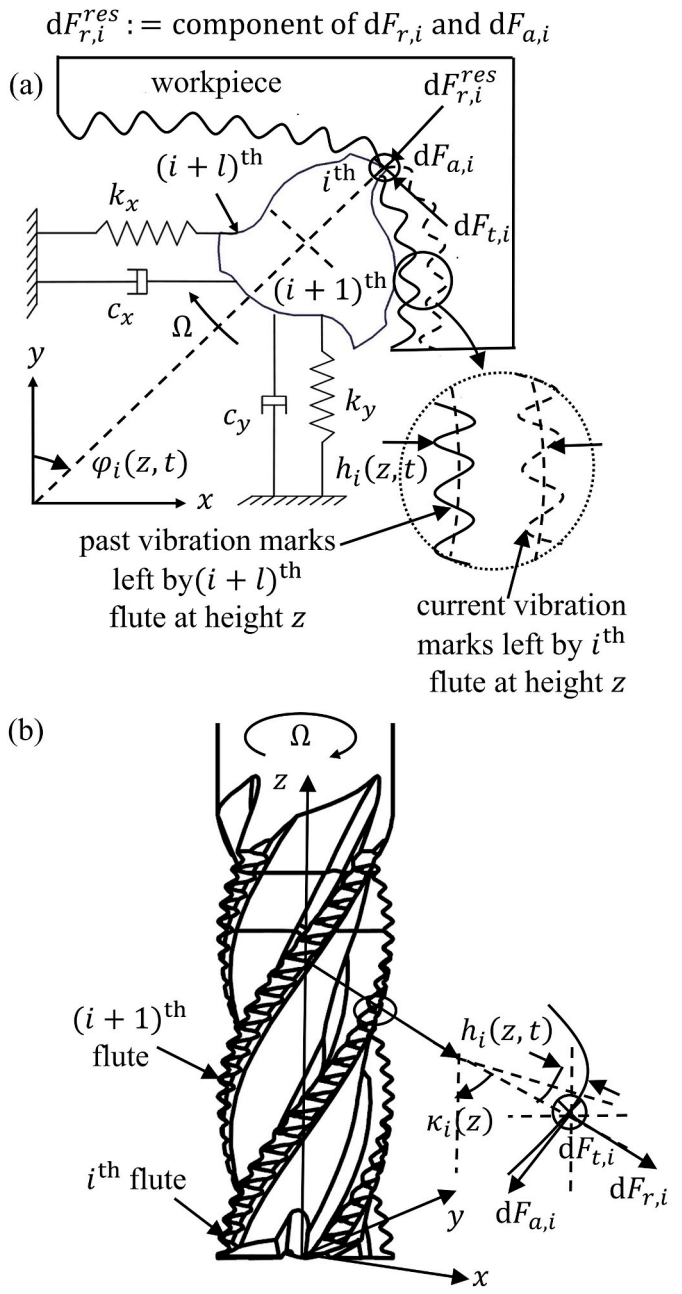

Fig. 1. (a) Cross-sectional schematic of a flexible serrated end mill imprinting vibrations on the workpiece, (b) side view showing the serration profile and some force components.

where, $\kappa_i(z)$ is the axial immersion angle, $dF^{dc}{}_{r,i}(z,t)$, $dF^{dc}{}_{t,i}(z,t)$, and $dF^{dc}{}_{a,i}(z,t)$ are elemental dynamic forces in the *rta* frame, $\mathbf{K}^c = [K_r^c \quad K_t^c \quad K_a^c]^T$ is the vector of primary cutting force coefficients, and $\mathbf{T}_{xr,i}(z,t) = \begin{bmatrix} -\sin\varphi_i\sin\kappa_i & -\cos\varphi_i & -\sin\varphi_i\cos\kappa_i \\ -\cos\varphi_i\sin\kappa_i & \sin\varphi_i & -\cos\varphi_i\cos\kappa_i \end{bmatrix}$ is the force transformation matrix with $\kappa_i := \kappa_i(z), \varphi_i := \varphi_i(z,t)$, where, $\varphi_i(z,t)$ is the radial immersion angle for the i^{th} flute at height z and time t.

Since the static chip thickness has no contribution to the regeneration mechanism, it is not included in Eq. (1), and only the elemental dynamic chip thickness, $h_i^{dc}(z,t)$ is retained since it causes vibrations of the tool. Transforming the dynamic displacements from the *xyz* to the *rta* frame, $h_i^{dc}(z,t)$ in the radial direction of the *rta* frame for the i^{th} flute at height z and time t can be shown to be:

$$h_i^{dc}(z,t) = [\sin\varphi_i(z,t)\sin\kappa_i(z) \quad \cos\varphi_i(z,t)\sin\kappa_i(z)] \begin{bmatrix} \Delta x \\ \Delta y \end{bmatrix} \times g_i(z,t), \tag{2}$$

where, $g_i(z,t)$ is a screening function, and $\Delta x := x(t) - x(t-\tau_i(z,t))$, $\Delta y := y(t) - y(t-\tau_i(z,t))$ represents the dynamic displacements in the x and y directions, respectively. $\tau_i(z,t)$ is the time delay at height z and time t between the current vibration made by the i^{th} flute and the past vibration made by the $(i+l)^{th}$ flute. Because of the variation in the local radius of these cutters, there can be a missed-cut effect which can result in a multiple delay term:

$$\tau_i(z,t) = \frac{\varphi_i(z,t) - \varphi_{(i+\nu_i(z,t)+1)}(z,t)}{\Omega}, \tag{3}$$

where, Ω is the spindle rotational speed (rad/sec), and $\nu_i(z,t)$ are the number of flutes skipped due to the missed-cut. Considering the case of tools with a non-uniform pitch and helix, the number of flutes skipped can be evaluated as [3,4]:

$$\nu_i(z,t)+1 = \text{find}(i_{new}) \rightarrow \min_{i_{new}=1}^{N} \left[(R_i(z) - R_{i+l}(z)) + f_{i,l}(z,t)\sin\varphi_i(z,t)\right]\sin\kappa_i(z), \tag{4}$$

where, N represents the number of teeth, $R_i(z)$ is the local radius for the i^{th} flute at height z, $f_{i,l}(z,t)$ is the feed per revolution between the i^{th} and $(i+l)^{th}$ flute which is detailed in Ref. [9], and $l = i_{new} - N$ if $i_{new} + i > N$, else $l = i_{new}$.

The total lumped dynamic cutting force vector acting on the cutting tool in the x and y directions is evaluated by integrating the differential force vector (in Eq. (1)) along the flute and summing the contribution of all flutes as:

$$\mathbf{F}_{xy}^{dc}(t) = \begin{bmatrix} F_x^{dc} & F_y^{dc} \end{bmatrix}^T = \sum_{i=1}^{N} \int_0^{a_p} d\mathbf{F}_{xy,i}^{dc}(z,t), \tag{5}$$

where, a_p is the axial depth of cut. Substituting Eqs. (1)–(4) into Eq. (5) and rearranging into a matrix form we get:

$$\mathbf{F}_{xy}^{dc}(t) = \sum_{i=1}^{N} \int_0^{a_p} \mathbf{A}_i(z,t) \begin{bmatrix} x(t) - x(t-\tau_i(z,t)) \\ y(t) - y(t-\tau_i(z,t)) \end{bmatrix}, \tag{6}$$

where, $\mathbf{A}_i(z,t)_{(2\times2)} = \begin{bmatrix} a_{xx,i}(z,t) & a_{xy,i}(z,t) \\ a_{yx,i}(z,t) & a_{yy,i}(z,t) \end{bmatrix}$ is the time-varying elemental directional dynamic milling force coefficient matrix for the i^{th} flute at height z and time t, elements of which can be shown to be:

$$\left.\begin{aligned} a_{xx,i}(z,t) &= g_i(z,t)\left[-K_a^c\cos\kappa_i\sin^2\varphi_i - K_r^c\sin\kappa_i\sin^2\varphi_i - K_t^c\cos\varphi_i\sin\varphi_i\right]dz \\ a_{xy,i}(z,t) &= g_i(z,t)\left[-K_t^c\cos^2\varphi_i - K_a^c\cos\kappa_i\cos\varphi_i\sin\varphi_i - K_r^c\sin\kappa_i\cos\varphi_i\sin\varphi_i\right]dz \\ a_{yx,i}(z,t) &= g_i(z,t)\left[K_t^c\sin^2\varphi_i - K_a^c\cos\kappa_i\cos\varphi_i\sin\varphi_i - K_r^c\sin\kappa_i\cos\varphi_i\sin\varphi_i\right]dz \\ a_{yy,i}(z,t) &= g_i(z,t)\left[K_t^c\cos\varphi_i\sin\varphi_i - K_r^c\sin\kappa_i\cos^2\varphi_i - K_a^c\cos\kappa_i\cos^2\varphi_i\right]dz \end{aligned}\right\} \tag{7}$$

These dynamic cutting forces govern the stability of serrated cutters. To characterize stability, the generalized equation of motion of the serrated cutter in the modal space can be described as [4,16]:

$$\ddot{\mathbf{q}}(t) + \mathbf{C}\dot{\mathbf{q}}(t) + \mathbf{K}\mathbf{q}(t) = \mathbf{M}^{-1}\mathbf{U}^T\mathbf{F}_{xy}^{dc}(t), \tag{8}$$

where, the modal displacement is $\mathbf{q}(t)_{m\times1} = \begin{bmatrix} \mathbf{q}_x(t)_{m_x\times1} \\ \mathbf{q}_y(t)_{m_y\times1} \end{bmatrix} = \mathbf{U}^T[x(t)\ y(t)]^T$, the modal damping matrix is $\mathbf{C}_{(m\times m)} = \text{diag}[2\zeta_r\omega_r]$, the modal stiffness matrix is $\mathbf{K}_{(m\times m)} = \text{diag}[\omega_r^2]$, the mode shape matrix is $\mathbf{U}_{(2\times m)} = \begin{bmatrix} [1\ 1\ldots1]_{(1\times m_x)} & [0\ 0\ldots0]_{(1\times m_y)} \\ [0\ 0\ldots0]_{(1\times m_x)} & [1\ 1\ldots1]_{(1\times m_y)} \end{bmatrix}$, and the inverse of the modal

mass matrix is $\mathbf{M}^{-1}{}_{(m\times m)} = \text{diag}\left[\left(\frac{\omega_r^2}{k_r}\right)\right]$, where, the subscript $r\,(=1,2,\ldots,m)$ is the mode number and total number of modes $m = m_x + m_y$. Furthermore, ζ_r is the modal damping ω_r, the modal frequency, k_r, the modal stiffness, and m_x and m_y are number of modes in x and y directions, respectively. Since the response in Eq. (8) depends on the previous displacement(s), Eq. (8) is a delay differential equation. Machining stability for such systems with multiple delays is characterized herein using frequency and time-domain methods. Generally, in the time domain, we need the system modal parameters (ω_r,ζ_r,k_r) which are extracted from the measured frequency response functions (FRF). In the frequency domain, measured or fitted FRFs could be used directly. However, it is also possible to use frequency domain FRF to solve the stability in the time domain as shown in Ref. [37].

3. Solving for stability using frequency and time-domain methods

This section details methods to solve for stability for serrated end mills that have distributed multiple delays using frequency and standard time-domain methods.

3.1. Frequency domain methods

Within the family of frequency domain solutions, we first present the generalized graphical method, followed by presenting solutions of zero-order approximation and the multi-frequency methods using the Nyquist criterion.

3.1.1. Generalized graphical method

Models presented here build on the methods originally proposed in Refs. [5,33] and address the shortcoming therein by generalizing to accommodate end mills with arbitrary serration profiles and those with non-uniform helix and pitch angles. We also discuss how the generalized models are valid for (non-)regular end mills. This generalization of the graphical method for stability analysis of serrated end mills is our new contribution to the state-of-the-art.

We demonstrate the workings of the graphical method with three examples. The first example is that of a three-fluted non-standard inclined circular profiled serrated cutter with uniform helix and pitch. The second example is that of a three-fluted non-standard semi-elliptical profiled serrated cutter with non-uniform helix and pitch, and the third example is that of a three-fluted standard trapezoidal profiled serrated cutter with uniform helix and pitch. These tools are chosen due to their different serration profiles; the trapezoidal profiled cutter is standard, and the inclined circular profile is more traditional when compared to the non-traditional, semi-elliptical profile. Geometry of these serrated cutters is complex, and since their geometry has already been described using parametric and NURBS-based representations as detailed in Ref. [9], Table 1 summarizes the geometry of these cutters.

In the graphical method, all cutting forces and effective displacements are defined along an average chip thickness direction ($\vec{\mathbf{n}}$) which passes through a plane perpendicular to the cutter's axis of rotation. Hence an average number of teeth in contact is considered. Furthermore, the vibration modes are also projected along $\vec{\mathbf{n}}$ to obtain oriented FRFs, much like was suggested in the 'average tooth angle approach' by Tlusty et al. [13]. As an example, the average chip thickness direction ($\vec{\mathbf{n}}$) for the case of slotting is shown in Fig. 2.

Stability analysis with the graphical method, like the other frequency domain methods [22,30] is conducted at the boundary of stability, i.e., where there is no increase or decrease in the amplitude of vibration, i.e.,

Table 1
Geometry of the non-standard serrated end mills of interest [9].

Cutter type	Serration parameters; Initial phase shift (ψ); helix angles (η); pitch angles ($\varphi_{p,i}(0)$); No. of teeth (N); Tool diameter (D);
Tool 1 - Inclined circular serrated cutter	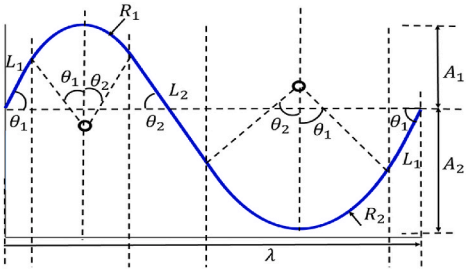 $A = 0.48$ mm; $R_1 = 0.52$ mm; $R_2 = 0.90$ mm; $\theta_1 = 40°$; $\theta_2 = 32°$; $\lambda = 2.27$ mm; $L_1 = 0.11$ mm; $L_2 = 0.33$ mm; $\psi = [0\ 120\ 240]°$ cw; $\eta = [38\ 38\ 38]°$; $\varphi_{p,i}(0) = [120\ 120\ 120]°$; $N = 3$; $D = 16$ mm .
Tool 2 - Semi-elliptical serrated cutter	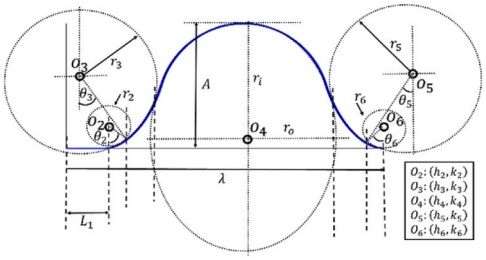 $A = 0.67$mm; $r_3 = 0.65$mm; $r_5 = 0.68$mm; $r_i = 0.47$mm; $r_o = 0.74$mm; $\lambda = 3.53$mm; $\theta_2 = 24°$; $\theta_3 = 64°$; $\theta_5 = 63°$; $\theta_6 = 25°$; $r_2 = 0.43$mm; $r_6 = 0.43$mm; $h_3 = 1.04$mm; $h_4 = 2.32$mm; $h_5 = 3.63$mm; $L_1 = 1.13$mm; $\psi = [0\ 120\ 240]°$ ccw; $\eta = [29\ 30\ 31]°$; $\varphi_{p,i}(0) = [117\ 122\ 121]°$; $N = 3$; $D = 16$ mm .
Tool 3 - Trapezoidal serrated cutter	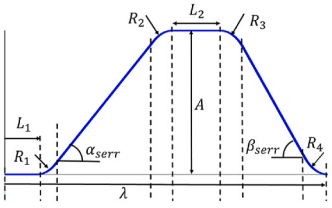 $A = 0.63$ mm; $L_1 = 0.97$ mm; $L_2 = 0$ mm; $R_1 = 0.06$ mm; $R_2 = 0.39$ mm; $R_3 = 0.39$ mm; $R_4 = 0.06$ mm; $\alpha_{serr} = 39$; $\beta_{serr} = 40$; $\lambda = 2.82$ mm; $\psi = [0\ 120\ 240]°$ cw; $\eta = [40\ 40\ 40]°$; $\varphi_{p,i}(0) = [120\ 120\ 120]°$; $N = 3$; $D = 16$ mm .

when $u(t) = u(t - \tau_i(z,t))$. This constant amplitude oscillation along $\vec{\mathbf{n}}$ is assumed to take the form of:

$$u(t) = u_0 \sin(\omega t - \phi), \tag{9}$$

where, u_0 is the amplitude of tool displacement, ω is the vibrational frequency, and ϕ is the phase lag between the resultant cutting force $F_{\text{res}}(t)$ and tool displacement response $u(t)$. The resulting cutting force is expressed as $F_{\text{res}}(t) = F\sin\omega t$, where the amplitude $F = \sqrt{\left(\left|F_x^{\text{dc}}\right|\right)^2 + \left(\left|F_y^{\text{dc}}\right|\right)^2}$. The resultant force $F_{\text{res}}(t)$ has two components: the non-regenerative force $F_{\text{n}}(t)$ and the regenerative force $F_{\text{r}}(t)$. The non-regenerative force $F_{\text{n}}(t)$ has a single component to represent the present dynamic force. The regenerative force $F_{\text{r}}(t)$ is formed of as many

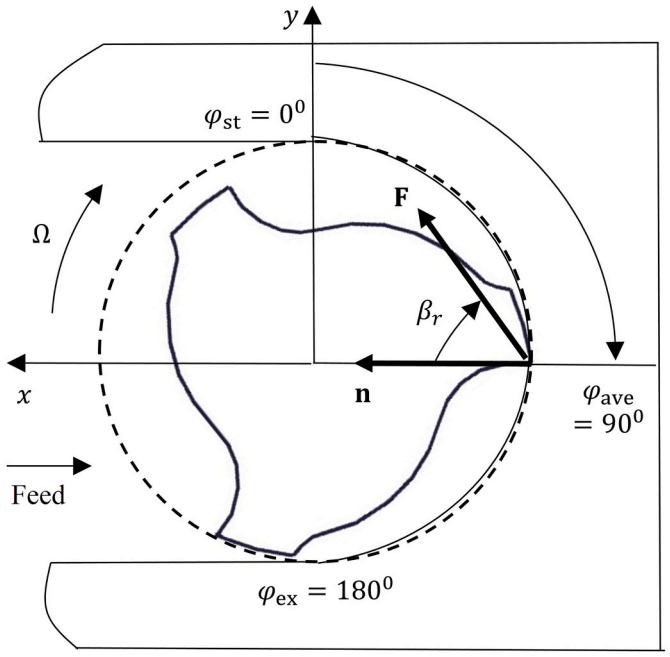

Fig. 2. Average chip thickness direction ($\vec{\mathbf{n}}$) for the case of slotting.

different components as the multiple time delays, each of which depends on the tooth that last machined the surface. A plot of these forces on the polar locus of the oriented FRF is used to derive expressions for the limiting stable depth of cut. The angle β_r ($= \tan^{-1}\frac{K_t^r}{K_r^r}$) between average chip thickness direction and resultant force (in Fig. 2) is used to calculate directional orientation factors to calculate the oriented FRF.

The procedure to obtain the stability boundary consists of three main steps that include estimating delays and regenerative forces (step 1), construction of the force polygon (step 2), followed by construction of the stability boundaries (step 3). In the first step, for the serration geometry of interest, we define the feed, the radial immersion and the speed. We then estimate the instantaneous chip cross-section from the time delays $\tau_i(z,t)$ evaluated from Eq. (3). Fig. 3 shows these chip cross sections for the three cutters of interest for an assumed feed of 0.05 mm/tooth/rev.

Since the regenerative force depends on the time delay, which in turn varies along the axis of the cutter ($\tau_i(z,t)$) we evaluate forces over the wavelength λ by discretizing it in L number of infinitesimal elements of the size $\delta a = \lambda/L$. From the delay matrix $\tau_i(z,t)$, we evaluate the elemental discrete delay for the j^{th} element ($j = 1, 2, \ldots L$) on the 1st flute at the time t_s as follows $\tau_j := \tau_1(z, t_s)$. Variations of delay between previous and present cut surfaces along these elements are shown in Fig. 3. For when the 1st flute does not cut the current surface, we consider $\tau_j = 0$. Due to the missed-cut effect, cutting occurs only in the grey portions – as highlighted in Fig. 3. The grey portions have lengths equal to: $a_1 + a_2 + a_3$. From Fig. 3, it is evident that there occur multiple-regenerations along the axis of the cutter. These regenerations could occur due to the previous cut surface made by any of the previous flutes or by the same flute in the previous rotation.

As an example for the case of three fluted inclined circular cutter with uniform helix and pitch (see Fig. 3(a)), the surface of the chip being cut by the 1st flute was machined in part by the same flute one revolution (i.e., $-T$) previously in the zone of length a_2, partly by the 2nd flute (i.e., $-\frac{T}{3}$ previously in the zone of length a_1), and partly by 3rd flute (i.e., $-\frac{2T}{3}$ previously in the zone of length a_3), where, T is spindle rotation period and $T = 2\pi/\Omega = 60/n$ where, n is the spindle speed (rpm). From the chip cross-section profile, we obtain the length of actual cutting zones for the inclined circular cutter as follows: $a_1 = 0.04\lambda$, $a_2 = 0.4\lambda$,

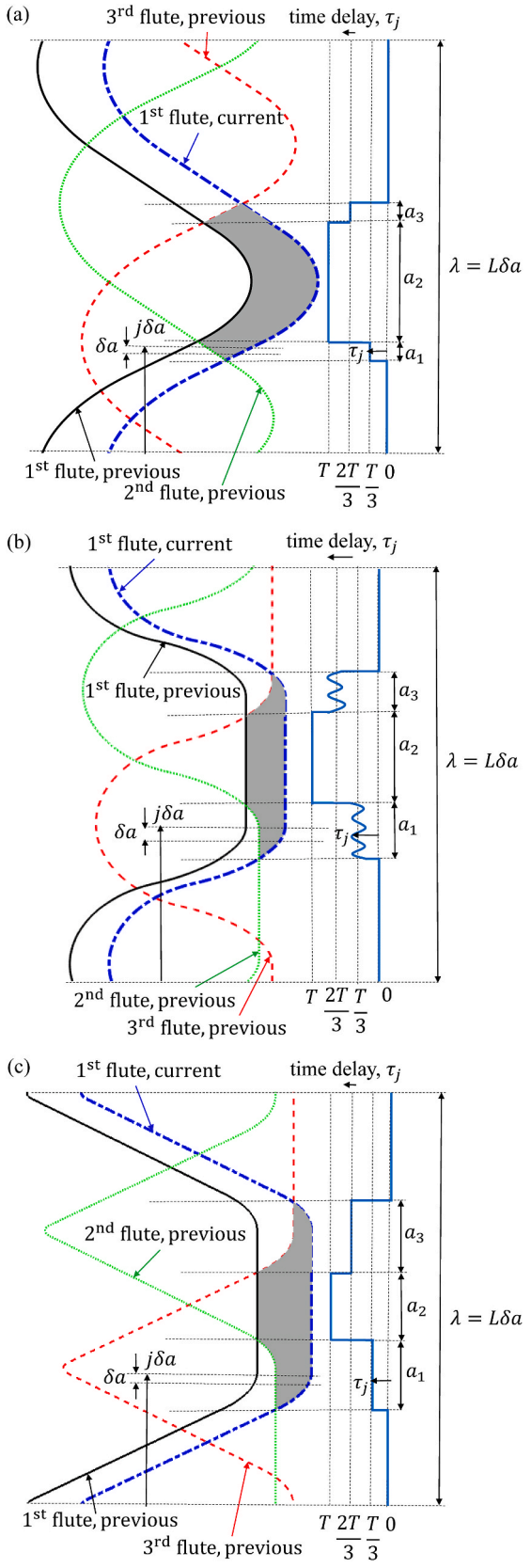

Fig. 3. Instantaneous chip cross-section (grey portion) and variation of delay period along the average chip thickness direction. Cutting conditions: Slotting with 0.05 mm/rev/tooth feed rate. Cutting tool: (a) 3-fluted inclined circular cutter with uniform helix and pitch, (b) 3-fluted semi-elliptical cutter with non-uniform helix and pitch, and (c) 3-fluted trapezoidal cutter with uniform helix and pitch.

$a_3 = 0.07\lambda$. The regenerative forces are formed only in these grey zones of different time lags. The non-regenerative forces are also active only in these grey zones, and depend only on the current vibration levels. Since the grey zones will change with feed, the non-regenerative and the regenerative force components also change with feed rate. Hence the total non-regenerative force $F_n(t)$ and the regenerative force $F_r(t)$ over the length λ are calculated similarly as follows:

$$F_n(t) = -K_s u_0(a_1 + a_2 + a_3)\sin(\omega t - \phi), \text{ and}$$
$$F_r(t) = K_s u_0\left[a_1 \sin\left(\omega t - \phi - \frac{\omega T}{3}\right) + a_2 \sin(\omega t - \phi - \omega T) + a_3 \sin\left(\omega t - \phi - \frac{2\omega T}{3}\right)\right], \tag{10}$$

where, $K_s(=\sqrt{K_t^{c2} + K_r^{c2}})$ is the resultant cutting force coefficient.

For uniform cutters τ_j between the 1st flute in the current cut and other flutes in the previous cut(s) is constant over all elements in each portion of the grey zones (see Fig. 3(a)). However, for the non-uniform cutter (see Fig. 3(b)), we see that τ_j between the current and previously cut elements on the 1st flute is T, τ_j between the current cut elements on the 1st flute and previous cut elements on the 2nd flute varies with a mean value of $\frac{T}{3}$, and τ_j between current cut elements on the 1st flute and previous cut elements on the 3rd flute varies with a mean value of $\frac{2T}{3}$. Knowledge of how τ_j varies is necessary to estimate the chip cross-section profile and the length of actual cutting zones which in turn are used to estimate the total forces.

For any serrated end mill, the total non-regenerative and the regenerative forces can be expressed in a generalized form by summing all elemental forces up to the serration wavelength ($\lambda = L\delta a$) as follows:

$$F_n(t) = \sum_{j=1}^{L} -\alpha_j K_s u_0 \delta a \sin(\omega t - \phi), \text{ and } F_r(t)$$
$$= \sum_{j=1}^{L} \alpha_j K_s u_0 \delta a \sin(\omega t - \phi - \omega\tau_j), \tag{11}$$

where, the screening function $\alpha_j = 1$ if $\tau_j > 0$ (grey, shaded portions) and $\alpha_j = 0$ if $\tau_j = 0$ (white portions, zero forces). Considering proportional forces, Eq. (11) is modified to calculate forces up to the depth of cut a_p as follows:

$$F_n(t) = -\sum_{j=1}^{L} K_s a_p u_0 \varepsilon_j \sin(\omega t - \phi), \text{and} F_r(t) \cong \sum_{j=1}^{L} K_s a_p u_0 \varepsilon_j \sin(\omega t - \phi - \omega\tau_j), \tag{12}$$

where, the ratio $\varepsilon_j = \alpha_j \frac{\delta a}{\lambda}$, and a_p is the depth of cut. For a 3-fluted uniform tool τ_j does not vary over axial discretized elements in the respective grey zones, and hence the summation of ε_j for all elements in the three portions of grey zones becomes $\frac{a_1}{\lambda}$, $\frac{a_2}{\lambda}$, and $\frac{a_3}{\lambda}$, respectively. In this case, for a uniform tool, multiplying Eq. (12) by λ/a_p reduces it to Eq. (10) which calculates the forces up to λ.

Having discussed how forces are evaluated, in the second step, those are plotted on the response locus of the oriented FRF as shown in Fig. 4, where, the length of each side of the force polygon is equal to the amplitude of the corresponding component of the resultant force. For a system with multiple modes, contribution of each vibration mode is summed in each direction to estimate an oriented FRF. Since the resultant force and displacement are calculated along the oriented FRF, around each vibration mode there will be a single response locus as shown in Fig. 4.

As can be seen in Fig. 4, the phase lag angle (ϕ) in between the resultant cutting force vector $F_{res}(t)$ and the displacement response vector $u(t)$ is decided by the frequency response at the tool tip. The non-regenerative force vector $F_n(t)$ is in opposite direction of this response vector $u(t)$. Considering relative phase angles, the components of regenerative force vector $F_r(t)$ are added to $F_n(t)$ to obtain the resultant force vector $F_{res}(t)$. From the force polygon, the angle between the non-regenerative force $F_n(t)$ and the resultant force $F_{res}(t)$ can be obtained as:

$$\tan\beta = \frac{\sum_{j=1}^{L} \varepsilon_j \sin(\omega\tau_j - \pi)}{\sum_{j=1}^{L} \varepsilon_j \{1 + \cos(\omega_c \tau_j - \pi)\}}. \tag{13}$$

Also, the amplitude F of resultant lumped force $F_{res}(t)$ for one flute can be written from the force polygon in Fig. 4 and from Eq. (12) as:

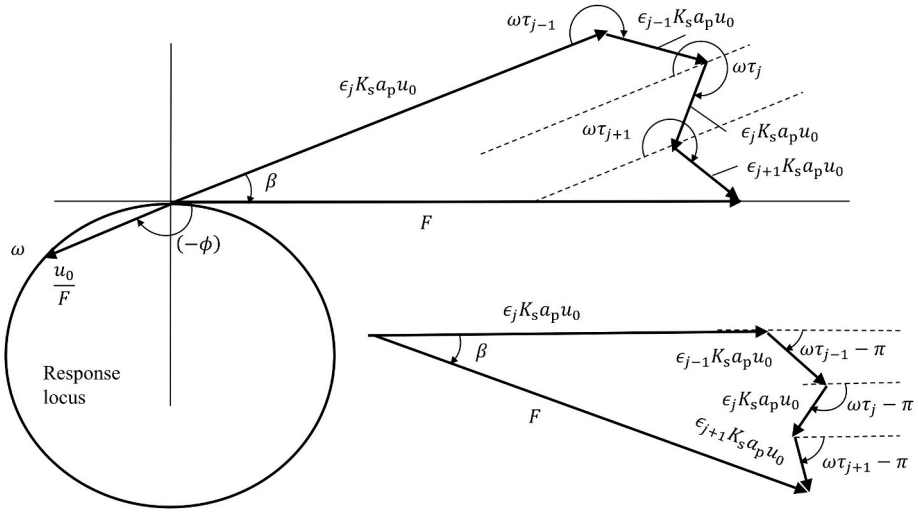

Fig. 4. Regenerative, non-regenerative and resultant forces plotted on the polar locus of the oriented FRF.

$$F = \frac{K_s a_p u_0}{\cos\beta}\left[\sum_{j=1}^{L} \varepsilon_j \{1 + \cos(\omega_c \tau_j - \pi)\}\right]. \tag{14}$$

Despite the chip thickness and force directions varying with time, along the flute and from one flute to another, the graphical method assumes that an 'average' number of teeth are in cut. Considering only those discretized elements of the cutter which cut the workpiece (when static chip thickness, $h_i^{st}(z,t) > 0$), the effective number of flutes (N_t) is calculated by integrating in-cut condition (σ_i) of each flute over the serration wavelength (λ) and spindle rotation period (T) as follows:

$$N_t = \frac{1}{\lambda T}\left[\sum_{i=1}^{N}\int_0^{\lambda}\int_0^{T} \sigma_i(z,t)\mathrm{d}t\mathrm{d}z\right],$$

and

$$\sigma_i(z,t) = \begin{cases} 1 & \text{if } h_i^{st}(z,t) > 0 \\ 0 & \text{otherwise} \end{cases}. \tag{15}$$

Then, the influence from all teeth is approximately calculated by multiplying the force on a single flute (Eq. (14)) by the effective number of flutes (N_t) over the contact zone to get the total force contributed by all flutes as follows: $F_{\text{total}} = N_t F$.

To construct the stability diagram, we check the phase angle ϕ in between the displacement and the resultant force as follows:

$$\tan\phi = \frac{\mathrm{Im}(H_{or}(j\omega))}{\mathrm{Re}(H_{or}(j\omega))}, \tag{16}$$

where, $H_{or}(j\omega)$ is the oriented FRF of the structure. For a particular spindle speed (n rpm) and given $H_{or}(j\omega)$, chatter frequency (ω_c rad/sec) is stored when the ϕ evaluated from Eq. (16) matches with the term $(\beta - \pi)$ obtained using Eq. (13). Putting $\frac{u_0}{F_{\text{total}}} = |H_{or}(j\omega)|$ in Eq. (14) and substituting $\omega = \omega_c$, the axial depth of cut $a_{p\text{lim}}$ at the stability boundary is obtained as follows:

$$a_{p_{\text{lim}}} = \frac{\cos\beta}{K_s N_t\left[\sum_{j=1}^{L}\varepsilon_j\{1 + \cos(\omega_c\tau_j - \pi)\}\right]\cdot|H_{or}(j\omega_c)|}. \tag{17}$$

The analytical expression in Eq. (17) is general and it is used for quick estimation of stability limit for any serrated cutter. By setting serration amplitude $A = 0$ mm, the same expression will be valid for the regular cutter with uniform/non-uniform pitch and helix. For a N fluted regular cutter with uniform pitch and helix, the phase angle relationship gives $\omega_c\tau_j = \frac{\omega_c T}{N} = 3\pi + 2\phi$. Also, as there is not any missed-cut, we get $\sum_{j=1}^{L}\varepsilon_j = \frac{a_1 + a_2 + a_3}{\lambda} = \frac{\lambda}{\lambda} = 1$ and hence Eq. (17) reduces to:

$$a_{p_{\text{lim}}} = \frac{\cos(\pi+\phi)}{K_s N_t[1 + \cos(2\pi + 2\phi)]|H_{or}(j\omega_c)|} = \frac{1}{2K_s N_t\cos(\pi+\phi)|H_{or}(j\omega_c)|} = \frac{1}{2K_s N_t \mathrm{Re}(H_{or}(j\omega_c))}. \tag{18}$$

This form of the limiting stable depth of cut for regular cutters is the same as given in Refs. [5,13]. For regular cutters with uniform pitch and helix, N_t in Eq. (18) is reduced to the following form $N_t = \frac{N(\varphi_{ex} - \varphi_{st})}{2\pi}$, where, φ_{ex} and φ_{st} are the exit and start angles, respectively.

In the graphical method, the actual multi-dimensional time-varying dynamics of serrated end milling is approximated to a single-dimensional time-invariant system. Hence the stability limit calculated by Eq. (17) is approximate. Although Eq. (17) is valid for 2-DOF system as well, it is not suitable for some cases which are discussed in Section 5.

Alternative frequency domain methods that transform the dynamic milling equations into time (in)variant but radial immersion-dependent systems are discussed next.

3.1.2. Zero-order approximation (ZOA) and multi-frequency solution (MFS)

In the zero-order approximation method [22] and the multi-frequency method [30] instead of using an 'average' number of teeth in cut, the time-varying coefficients ($\mathbf{A}_i(z,t)$) of the dynamic milling equations (see Eq. (6)) that depend on the angular orientation of the tool as it rotates through the cut are expanded into a Fourier series. The ZOA method retains only the average component of the Fourier series thus making the equations time invariant but radial immersion-dependent, whereas the MFS method retains higher order harmonics of the Fourier series. In both methods, the dynamic cutting forces are first transformed from the time (t) domain to the frequency (ω) domain by taking a Fourier transform of Eq. (6) as follows:

$$\Im\left\{\mathbf{F}_{xy}^{dc}(t)\right\} = \sum_{i=1}^{N}\int_0^{a_p}\Im\{\mathbf{A}_i(z,t)\}^{*}\Im\left\{\begin{bmatrix} x(t) - x(t-\tau_i(z,t)) \\ y(t) - y(t-\tau_i(z,t))\end{bmatrix}\right\} \tag{19}$$

We can further write the Fourier transform of dynamic displacement as:

$$\Im\left\{\begin{bmatrix} x(t) - x(t-\tau_i(z,t)) \\ y(t) - y(t-\tau_i(z,t))\end{bmatrix}\right\} = b_i^0(\omega,z)\Im\left\{\begin{bmatrix} x(t) \\ y(t)\end{bmatrix}\right\}, \tag{20}$$

where, the regenerative coefficient is $b_i^0(\omega,z) = \frac{1}{T}\int_0^T[1 - e^{-j\omega\tau_i(z,t)}]dt$ and ω is the vibration frequency. The instantaneous delay period $\tau_i(z,t)$ depends on the tool's serration profile and the pitch/helix angles. Fig. 5 demonstrates the normalized delay for the three fluted tool with semi-elliptical serration (in Table 1). For more convenient visualisation, the delay period is normalized by dividing the delay period by the tooth-passing period:

$$\tau_{n,i}(z,\varphi) = \frac{\tau_i(z,\varphi)}{T_s} \tag{21}$$

where, the normalized delay $\tau_{n,i}(z,\varphi)$ is plotted as a function of immersion angle (φ) and serration height (z) for each flute (i), and T_s ($= 2\pi/\Omega N$) is the tooth-passing period (sec). Hence the normalized delay is independent of spindle speed. In Fig. 5, normalized delay $\tau_n = 3$ means actual time delay $\tau = 3T_s = T$, where, T_s is tooth passing period, and T is spindle period and it suggests that the previous cut surface will be made by the same flute as the current one. Similarly, $\tau_n = 2$ means $\tau = 2T_s = 2T/3$ and the previous cut surface will be made by two flutes previously, and $\tau_n = 1$ means $\tau = T_s = T/3$ and the previous cut surface will be made by one flute previously. Also, the delay is zero for each flute at some particular heights where, the cutting does not occur due to the missed cut effect.

The stability analysis of Eq. (19) then proceeds by equating the frequency domain vibrations with the product of the FRF matrix and the frequency domain representation of cutting forces to result in the dynamic milling force equation in the frequency domain:

$$\Im\left\{\mathbf{F}_{xy}^{dc}(t)\right\} = \sum_{i=1}^{N}\int_0^{a_p}\mathbf{A}_i(z,\omega)^{*}\left[b_i^0(\omega,z)\mathbf{H}(j\omega)\Im\left\{\mathbf{F}_{xy}^{dc}(t)\right\}\right], \tag{22}$$

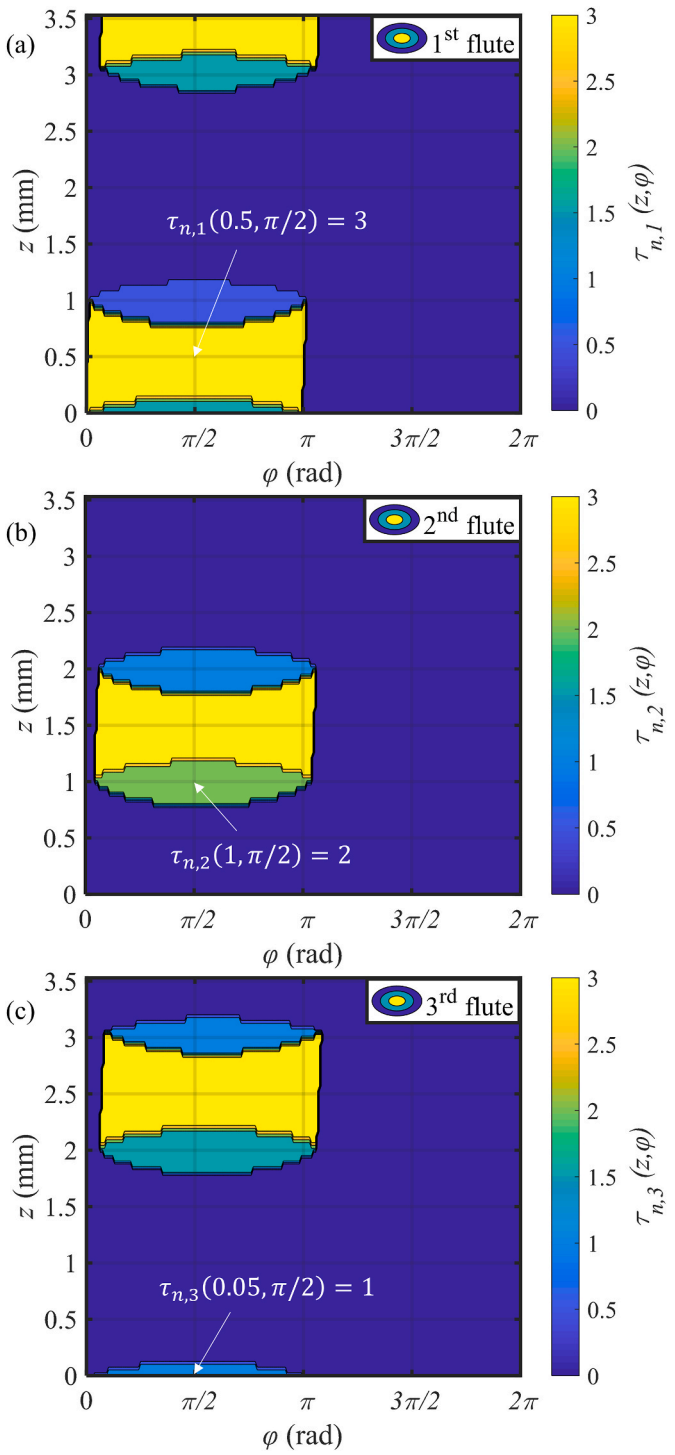

Fig. 5. Variation of normalized delay $\tau_{n,i}(z,\varphi)$ with axial height (z) and radial angle (φ) of the corresponding flute (i). Cutting tool: 3 fluted semi-elliptical serrated cutter with non-uniform pitch/helix. Cutting conditions: Slotting, and 0.05 mm/tooth/rev feed rate.

where, $\mathbf{H}(j\omega)=\begin{bmatrix} H_{xx}(j\omega) & H_{xy}(j\omega) \\ H_{yx}(j\omega) & H_{yy}(j\omega) \end{bmatrix}$ is the FRF matrix with direct FRFs, i.e., $H_{xx}(j\omega)$ and $H_{yy}(j\omega)$ and cross FRFs i.e., $H_{xy}(j\omega)$ and $H_{yx}(j\omega)$.

The varying delay with non-cutting sections is the main characteristic of serrated tool geometry which introduces modulation at spindle rotation frequency and its harmonics. Hence the directional coefficient matrix $\mathbf{A}_i(z,\omega)$ becomes periodic at spindle rotation frequency ($\Omega = 2\pi n/60$ rad/sec) and it can be approximated by a Fourier series:

$$\mathbf{A}_i(z,\omega)=\mathfrak{F}\{\mathbf{A}_i(z,t)\}=\sum_{r=-\infty}^{r=+\infty}\mathbf{A}_{i,r}(z)\delta(\omega-r\Omega),$$
$$\text{where, } \mathbf{A}_{i,r}(z)=\frac{1}{T}\int_0^T\mathbf{A}_i(z,t)e^{-jr\Omega t}\mathrm{d}t. \tag{23}$$

The number of harmonics (r) of the spindle rotation frequency to be considered for an accurate reconstruction of $\mathbf{A}_i(z,\omega)$ depends on the immersion conditions and on the number of teeth in the cut. For a fast prediction, following the zero-order approximation method [22], we retain only the average component of the Fourier series, i.e., the case with $r=0$:

$$\mathbf{A}_i^0(z)=\frac{1}{T}\int_0^T\mathbf{A}_i(z,t)\mathrm{d}t. \tag{24}$$

where, $\mathbf{A}_i^0(z)$ is the mean dynamic force coefficients' matrix which is time invariant but depends on the radial immersion. When the system is critically stable and vibrating at a chatter frequency ω_c, the roots of the characteristic equation (obtained from manipulating Eq. (22) as described in Ref. [22]) are obtained from the determinant of:

$$\det[\mathbf{I}_{(2\times2)}-\mathbf{\Lambda}\mathbf{H}(j\omega_c)]=0, \tag{25}$$

where, $\mathbf{\Lambda}$ is expressed as follows:

$$\mathbf{\Lambda}=\sum_{i=1}^{N}\int_0^{a_p}\mathbf{A}_i^0(z)b_i^0(\omega_c,z) \tag{26}$$

Since we have a system with multiple and distributed delays, an analytical and explicit expression for the limiting stable axial depth of cut a_p from $\mathbf{\Lambda}$ is not as straight-forward as it is for the case of a system with a constant delay [22]. And since separating $\mathbf{\Lambda}$ into its real and imaginary parts is also not feasible, a relationship between the chatter frequency and the spindle speed like for the case of the constant delay is also not possible [22]. Since analytical solution is not possible, and since the iterative search method takes a long simulation time as in Ref. [23], we solved the characteristic equation using the Nyquist stability criterion, as was also done in other contemporary work [24].

The Nyquist plot maps the Nyquist contour of the characteristic equation onto a complex plane. For a fixed spindle speed, axial depth of cut, and other cutting conditions, the process is unstable when any zero of the characteristic equation $\mathrm{CH}(j\omega)=\det\left[\mathbf{I}_{(2\times2)}-\mathbf{\Lambda}\mathbf{H}(j\omega)\right]$ creates a clockwise encirclement of the origin in the complex plane. Since an encirclement of the origin would require a crossing of the negative real axis, we check for stability using the method outlined in Ref. [35]. This method can handle multiple and distributed delays. And since the ZOA method approximates the time periodic milling system by a time invariant one, it is expected to be computationally efficient. However, the use of the average directional factor makes this method inaccurate for intermittent cutting that is a characteristic of serrated tools. Therefore, we further extend the use of the Nyquist check for stability to Eq. (23) that considers the case of multiple harmonics.

According to the Floquet theory, periodic forces $\mathbf{F}_{xy}^{dc}(t)$ have the following solution $\mathbf{F}_{xy}^{dc}(t)=e^{qt}\mathbf{E}(t)$. As the function $\mathbf{E}(t)$ is periodic at spindle rotation frequency Ω, we obtain the following form of the solution by putting $q=j\omega_c$ at the critical chatter limit:

$$\mathbf{F}_{xy}^{dc}(t)=e^{j\omega_c t}\mathbf{E}(t),\ \mathbf{E}(t)=\sum_{l=-\infty}^{l=+\infty}\mathbf{E}_l\,e^{jl\Omega t}. \tag{27}$$

Taking a Fourier transform of Eq. (27) and using modulation theorem, we obtain:

$$\Im\left\{\mathbf{F}_{xy}^{\mathrm{dc}}(t)\right\} = \Im\left\{e^{j\omega_c t}\mathbf{E}(t)\right\} = \sum_{l=-\infty}^{l=+\infty}\mathbf{E}_l\,\delta[\omega-(\omega_c+l\Omega)], \tag{28}$$

where, $\delta[\omega-(\omega_c+l\Omega)]$ is the Dirac delta function. Substituting Eq. (28) into Eq. (22) we get:

$$\Im\left\{\mathbf{F}_{xy}^{\mathrm{dc}}(t)\right\} = \sum_{i=1}^{N}\int_0^{a_p}\mathbf{A}_i(z,\omega)^*\left\{b_i^0(\omega,z)\mathbf{H}(j\omega)\sum_{l=-\infty}^{l=+\infty}\mathbf{E}_l\,\delta[\omega-(\omega_c+l\Omega)]\right\} \tag{29}$$

Using Eq. (23) and following procedures as outlined in Refs. [29,38], the Fourier coefficients of the dynamic forces can be expressed as follows:

$$\mathbf{E}_r = \sum_{l=-\infty}^{l=+\infty}\mathbf{\Lambda}_{r,l}\times\mathbf{H}(j(\omega_c+l\Omega))\mathbf{E}_l\,,\ldots(r,l)=0,\pm1,\pm2,..\pm\infty. \tag{30}$$

where, $\mathbf{\Lambda}_{r,l} = \frac{1}{T}\sum_{i=1}^{N}\int_0^{a_p}\int_0^{T} b_i^0((\omega_c+l\Omega),z)\mathbf{A}_i(z,t)e^{-j(r-l)\Omega t}\mathrm{d}t$, and where, b_i^0 is the same as it was in Eq. (26). The infinite dimension of Eq. (30) is truncated by usually considering only a finite number of harmonics. If, for example, only the first harmonic of the periodic function is considered (i.e., $(r,l)=0,\pm1$), the roots of the equality Eq. (30) are found from the condition of the non-trivial solution as follows:

$$\det\left[\mathbf{I}_{(6\times6)}-\mathbf{\Lambda H}(j(\omega_c+l\Omega))\right]=0,$$

where,

$$\mathbf{\Lambda} = \begin{bmatrix}\mathbf{\Lambda}_{0,0} & \mathbf{\Lambda}_{0,-1} & \mathbf{\Lambda}_{0,1}\\ \mathbf{\Lambda}_{-1,0} & \mathbf{\Lambda}_{-1,-1} & \mathbf{\Lambda}_{-1,1}\\ \mathbf{\Lambda}_{1,0} & \mathbf{\Lambda}_{1,-1} & \mathbf{\Lambda}_{1,1}\end{bmatrix} \tag{31}$$

Since the system has multiple and distributed delays, iterative solutions for $\mathbf{\Lambda H}(j\omega_c+l\Omega)$ to find relationships for critical depths of cut, speeds, and chatter frequencies are not feasible as they are for the case of a system with a constant delay [30]. And, instead of using the cumbersome root finding technique suggested in Ref. [31], like we did for the ZOA method with distributed delays, herein too we use the Nyquist criterion to characterize the stability of the system. Since the Nyquist check is not iterative, it is expected to be computationally more efficient than the iterative solution. The computational effort will however depend on the number of harmonic components considered to represent the periodic function. The MFS method keeps the time varying system parameters, so it is expected to accurately predict stability for serrated end mills with highly intermittent force characteristics – as is discussed in Section 4. Our use of the Nyquist stability criterion for stability checks is limited to the single-input-single-output (SISO) systems, i.e., for the dynamic response to the cutting force at the cutting point of interest.

Our stability solution of systems with multiple and distributed delays through the multi-frequency solution method is a new contribution to the literature in which prior work was limited to the use of Nyquist stability criterion for stability analysis of systems with constant delays. Since the solution approaches with the graphical method, ZOA and the MFS methods are all novel for serrated tools, we benchmark predictions with established time domain methods that are briefly outlined next.

3.2. Time-domain methods

Time-domain methods handle the delay differential equations with distributed delays with ease, without the need for 'averaging' and/or approximating delays. These methods have hence been preferred in earlier research concerned with characterizing stability of serrated end mills [2,4,13–19]. The time domain methods used earlier were based on numerical integration schemes [14,18] and on using the more computationally efficient semi-discretization method [4,20]. And, since details are available elsewhere, we outline only the key steps herein.

3.2.1. Time-domain Euler integration method

In this method, we first evaluate the elemental total chip thickness $h_i(z,t) = h_i^{\mathrm{st}}(z,t) + h_i^{\mathrm{dc}}(z,t)$ using the vibration of the current and previous cut(s) at the selected tooth angle. Thereafter the total lumped cutting forces ($\mathbf{F}_{xy}(t) = \mathbf{F}_{xy}^{\mathrm{st}}(t) + \mathbf{F}_{xy}^{\mathrm{dc}}(t)$, where, $\mathbf{F}_{xy}^{\mathrm{st}}(t)$ are the static forces [8,9]) are evaluated. These forces are used to find new displacements in the x and y directions using Euler integration. Displacements are obtained using the procedure detailed in Refs. [14,18] by solving for the response using the second order equations of motion of the form shown in Eq. (8). The tooth angle is then incremented, and the process is repeated. The time step for integration is set to be at least ten times smaller than the period corresponding to the highest natural frequency of interest. Simulated time history data of the displacements $(x(t),y(t))$ are used to evaluate stability. The stability is evaluated by the metric M which is the normalized sum of the difference between subsequent points of the once-per-spindle revolution sampled data [18]. At a stable cutting condition, sampled points repeat in every revolution, and hence M remains zero. Whereas for an unstable cut, the points do not repeat and hence M is greater than zero. To characterize the transition from the stable to the unstable zone (defined by a_{plim}) at a particular speed (n) we gradually increase the depth of cut (a_p) until $M>0$. Since this method requires us to scan several depths of cut at all speeds of interest, and every simulation proceeds until the cut is deemed stable or not, this method is computationally very intensive.

3.2.2. Semi-discretization method

The semi-discretization method discretizes the delayed states while leaving the actual time domain terms unchanged. The method is hence computationally more efficient than the standard time domain numerical integration schemes. The method requires that the standard form of the delay differential equation (Eq. (8)), is decomposed to the first order form as follows [20]:

$$\dot{\mathbf{Q}}(t) = \mathbf{L}(t)\mathbf{Q}(t) + \sum_{i=1}^{N}\int_0^{a_p}\mathbf{B}_i(z,t)\mathbf{V}(t-\tau_i(z,t)), \text{and } \mathbf{V}(t) = \mathbf{DQ}(t), \tag{32}$$

where, $\mathbf{Q}(t)_{(2m\times1)} = [\mathbf{q}(t)\quad \dot{\mathbf{q}}(t)]^T$, $\mathbf{D}_{(2m\times2m)} = \mathbf{I}_{(2m\times2m)}$,

$\mathbf{A}(t)_{(2\times2)} = \sum_{i=1}^{N}\int_0^{a_p}[\mathbf{A}_i(z,t)]$, $\mathbf{L}(t)_{(2m\times2m)} = \begin{bmatrix}\mathbf{0}_{(m\times m)} & \mathbf{I}_{(m\times m)}\\ \mathbf{M}^{-1}\mathbf{U}^{\mathrm{T}}\mathbf{A}(t)-\mathbf{K} & -\mathbf{C}\end{bmatrix}$,

$\mathbf{B}_i(z,t)_{(2m\times2m)} = \begin{bmatrix}\mathbf{0}_{(m\times m)} & \mathbf{0}_{(m\times m)}\\ -\mathbf{M}^{-1}\mathbf{U}^{\mathrm{T}}\mathbf{A}_i(z,t) & \mathbf{0}_{(m\times m)}\end{bmatrix}$

Following the semi-discretization technique for the case of stability with multiple delays as given in Ref. [20], we can determine the transition matrix $\mathbf{\Phi}$ over the principal period T. According to the Floquet Theory, the system is asymptotically stable if the modulus of eigenvalues of $\mathbf{\Phi}$ (i.e., the characteristic multipliers) is equal to one, stable if the modulus of the eigenvalues is less than one, and unstable if the modulus of the eigenvalues is greater than one. In this method too, for every spindle speed of interest, the axial depths of cut are increased in steps and the stability is evaluated at each combination of speed and depth of cut. The computational efficiency of this method depends on the number of discretization steps, for which, usually a convergence study is necessary to optimize the time step size [39].

4. Benchmarking of proposed models and experimental validation

We present here the experimental validation of predicted stability behavior for the three cutters of interest (see Table 1). We also benchmark results obtained with proposed graphical and frequency domain methods with those obtained using the established high-fidelity time

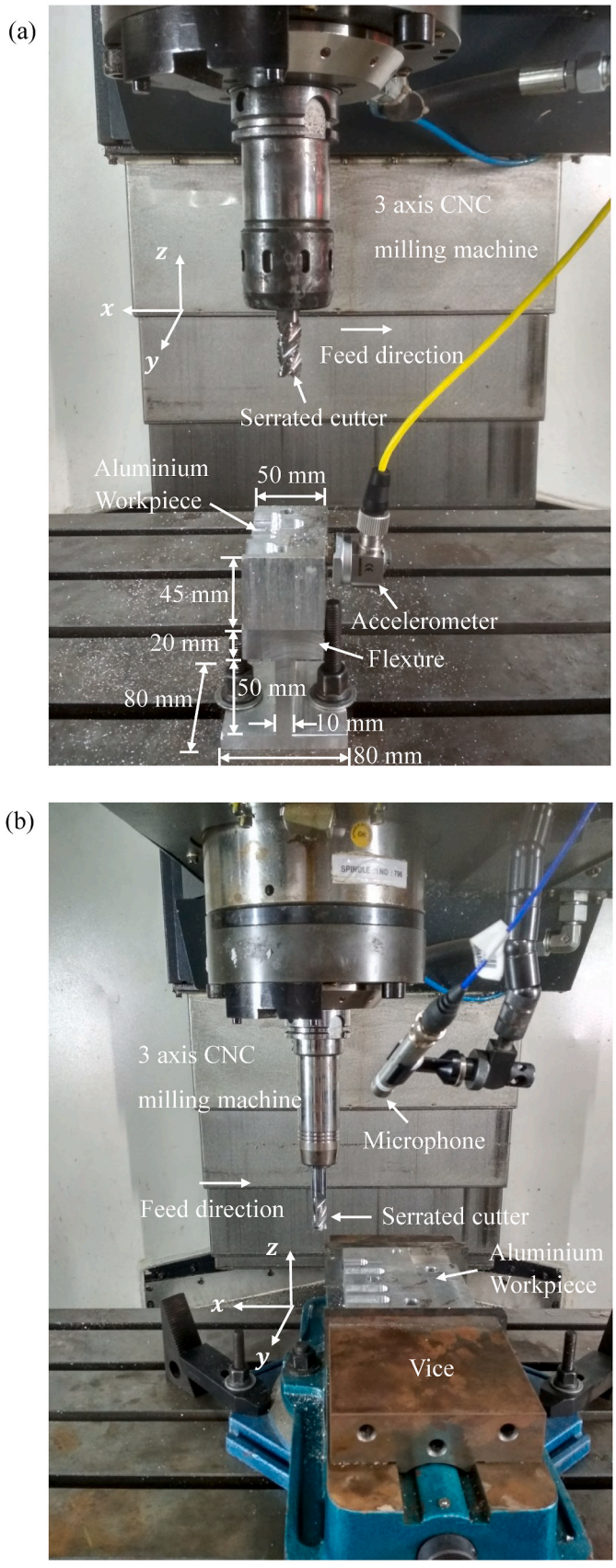

Fig. 6. Experimental setups for validating stability behavior for (a) the two non-standard serrated cutters with the workpiece-flexure system being more flexible than the tool, (b) the standard trapezoidal profiled cutter with the tool being more flexible than the workpiece mounted in a vice.

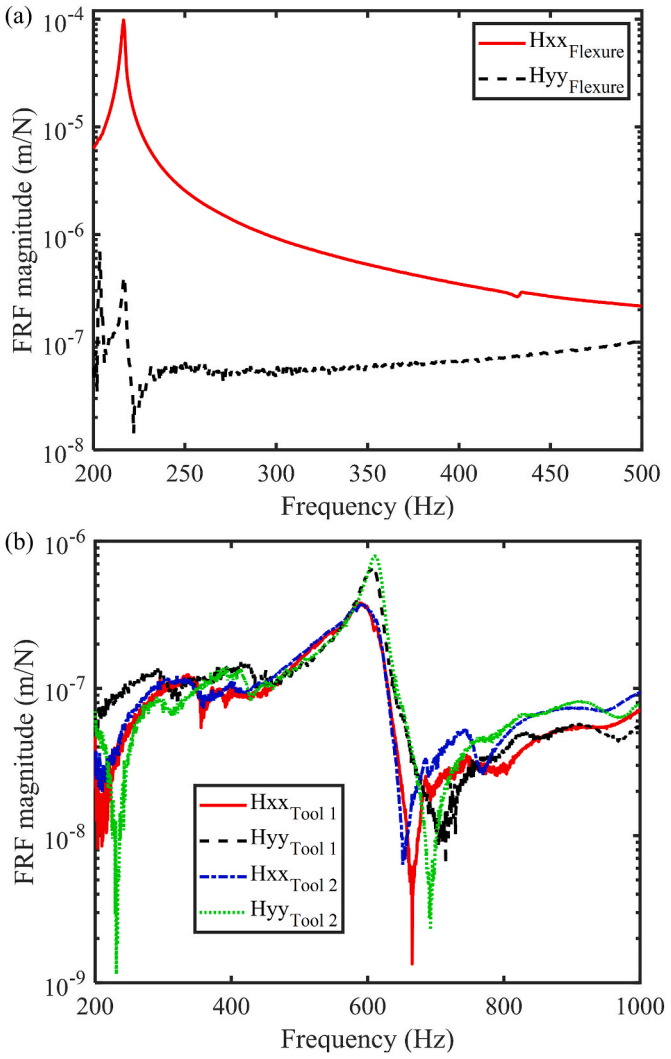

Fig. 7. Measured FRFs for (a) the workpiece-flexure system, (b) Tool 1 (inclined circular serrated cutter) and Tool 2 (semi-elliptical serrated cutter) in the x and y directions.

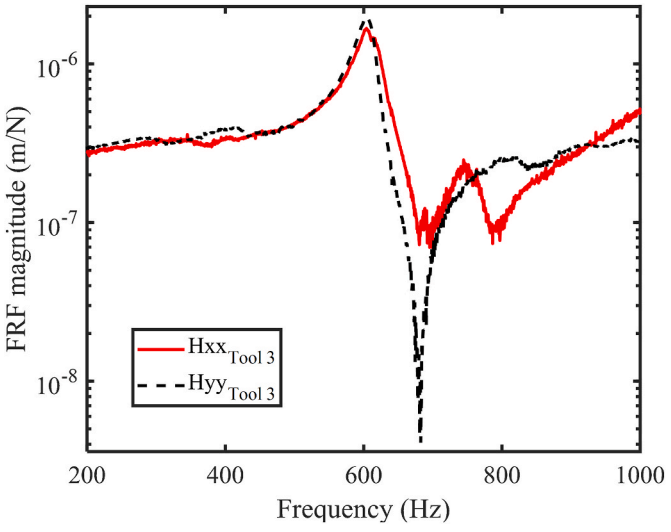

Fig. 8. Measured direct FRFs for Tool 3 (trapezoidal profiled serrated cutter) in its x and y directions.

domain methods.

All experiments were conducted on a three-axis AMS make CNC vertical milling machine. As shown in Fig. 6, we used two experimental setups. First setup was to experimentally validate stability behavior of the two non-standard profiled serrated cutters. As shown in Fig. 6(a), the workpiece was mounted on a web-shaped flexure using two M5 screws housed in a counterbore. The workpiece-flexure system was designed to behave like a single degree-of-freedom system with its main flexibility in the x-direction, i.e., along the feed direction. Use of such specially designed web shaped flexures is not unusual for validating stability models, and our design was informed by other reported work [18,40]. The tools of the first setup were mounted in a power chuck type tool holder and the overhang of the tool was kept short to ensure the tool was dynamically much stiffer than the flexure.

A different setup was used to additionally validate our stability models for the case of the tool being more flexible than the workpiece, i.e., the usual case of machine tools. As shown in Fig. 6(b), this second setup was used to experimentally validate stability behavior of the standard trapezoidal profiled serrate cutter. In this case, the workpiece was rigidly fixed in a vice and the tool was mounted in a flexible hydrogrip type holder. In this case the tool was flexible in the x and y directions and workpiece was much stiffer than the tool.

Dynamics in both cases were measured using a modal hammer (DYTRAN 5800B4) and a single-axis accelerometer (DYTRAN 3225F1). For the setup shown in Fig. 6(a), we measured dynamics of the workpiece-flexure system and of the two different tools in both the x and y directions. These measured dynamics characterized by their receptance FRFs are shown in Fig. 7. For the setup shown in Fig. 6(b) we only measured the dynamics of the tool in the x and y directions, and those FRFs are shown in Fig. 8. For all measurements, data acquisition and modal curve fitting were conducted using CutPro® [41].

As is evident from the FRFs in Fig. 7, the response of the workpiece-flexure system in the x-direction is almost two orders of magnitude more flexible than its behavior in the y-direction and/or the modes of both tools of interest. The workpiece-flexure system can hence be approximated as a single degree of freedom system whose modal parameters were identified to be: $f_x = 216.5$ Hz, $\zeta_x = 0.4\%$, $k_x = 1.32 \times 10^6$ N/m. FRFs in Fig. 8 show that the tool has one dominant vibration mode in each of its x and y directions, and that these are both more flexible than the tool modes shown in Fig. 7(b). Modal parameters for this tool (tool 3) were identified to be: $f_x = 604.5$ Hz, $\zeta_x = 1.7\%$, $k_x = 1.68 \times 10^7$ N/m and $f_y = 603.7$ Hz, $\zeta_y = 1.67\%$, $k_y = 1.49 \times 10^7$ N/m.

For all sets of experiments, we slot milled Aluminium (Al7075) with mechanistically identified primary cutting force coefficients of: $K_t^c = 824$ N/mm^2, $K_r^c = 225$ N/mm^2, $K_a^c = 15$ N/mm^2, and edge cutting force coefficients of: $K_t^e = 24$ N/mm, $K_r^e = 28$ N/mm, $K_a^e = 2$ N/mm. The workpiece mounted on the flexure and in the vice was not changed during experiments. The main purpose was to validate the stability behavior. Since the ratio of chip load to the serration amplitude influences stability behavior, the feed rate for all experiments was fixed to be 0.05 mm/tooth/rev. Once models were validated, the influence of feed rate on stability was separately investigated.

For the setup shown in Fig. 6(a) a uniaxial accelerometer was used to measure the vibration of the workpiece-flexure system during cutting, whereas a microphone was used to monitor the cutting process for the setup shown in Fig. 6(b). A stable cut was classified as that in which the FFT of the response signal was dominated by the spindle frequency or tooth passing frequency and/or its harmonics. The chatter case was classified as that in which the FFT of the response signal was dominated by a peak close to the natural frequency of system and one that is not a harmonic of the spindle frequency and/or the tooth passing frequency. Additionally, where necessary, the case of chatter was also confirmed by sampling signals at once-per-revolution (i.e., at the spindle rotating

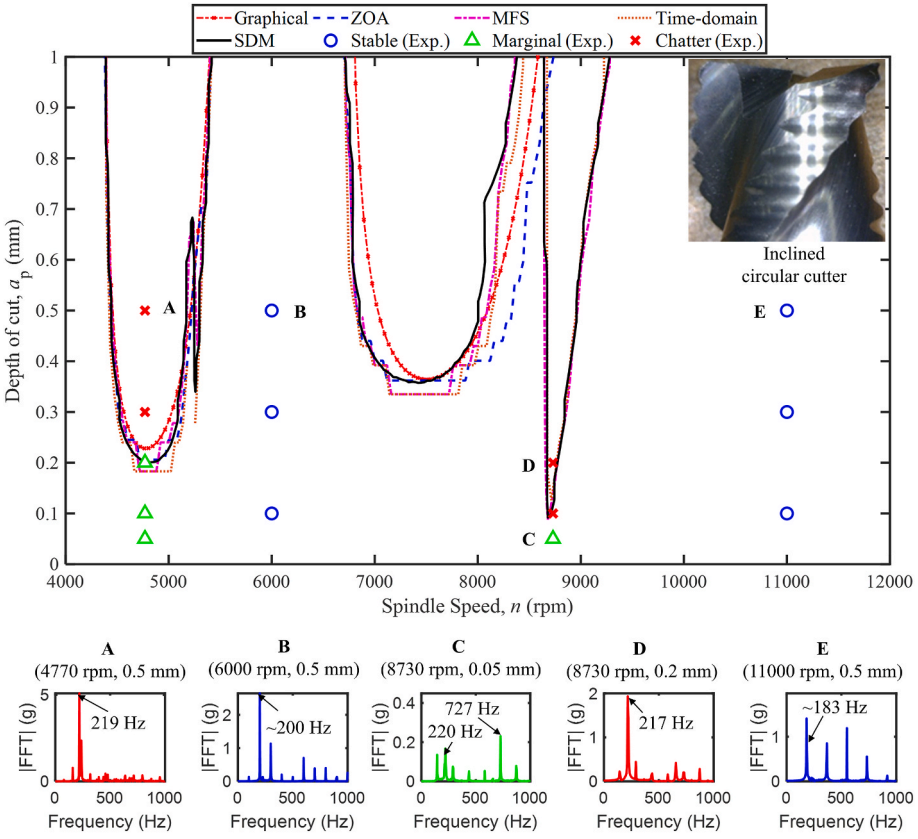

Fig. 9. Stability behavior for the three-fluted non-standard profiled inclined circular serrated cutter with uniform pitch and helix for slot cutting with 0.05 mm/tooth/rev feed rate. Experiments were conducted on the setup shown in Fig. 6(a).

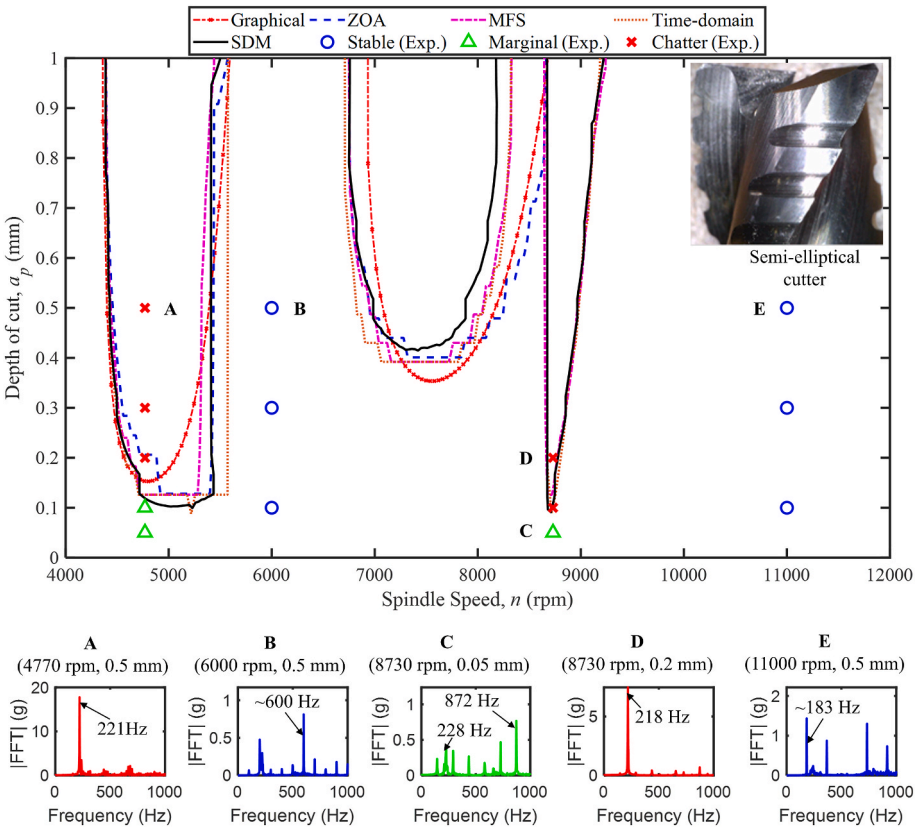

Fig. 10. Stability behavior for the non-standard profiled semi-elliptical serrated cutter with non-uniform pitch and helix for slot cutting with 0.05 mm/tooth/rev feed rate. Experiments were conducted on the setup shown in Fig. 6(a).

frequency). This periodic sampling approach was used to confirm if the milling response was synchronous (or not) with the spindle rotation; if synchronous, the cut is deemed stable, and if not, the cut is deemed unstable [18]. Conditions at which chatter was not fully developed were classified as transition regions between the stable and the unstable case, and these cases were identified as those in which the FFT of the response contained the spindle frequency or the tooth passing frequency and/or its harmonics as well as a peak of relatively lower magnitude close to the natural frequency of the system.

Fig. 9 shows results for the three-fluted inclined circular serrated cutter with uniform pitch and helix. Fig. 10 shows results for the three-fluted non-standard semi-elliptical profiled serrated cutter with non-uniform helix and pitch. Fig. 11 shows results for the three-fluted standard trapezoidal profiled serrated cutter with uniform pitch and helix.

Model predictions include results obtained using the proposed graphical method, and the results obtained using the rapid solution with ZOA and the MFS methods. For the MFS method, three harmonics ($r,l = 3$) were considered. This was decided based on the spectra of the static feed force being dominated by three harmonics, and by also checking for how many harmonics were necessary to capture the critical depths of cut in the period-doubling (flip) lobes. Since the frequency step affects simulation time in ZOA/MFS, it was set at 0.5 Hz in the frequency range from 216.5 Hz to 236.5 Hz for the case in which the workpiece-flexure system is flexible. The frequency range from 590 Hz to 650 Hz was considered for simulating the case with the tool being more flexible. For further reduction of simulation time, the speed-independent delay (divided by tooth passing period) was calculated beforehand for each depth of cut in the range. Moreover, for the case of the MFS solutions, to further improve computational efficiency, the $\mathbf{\Lambda}$ and $\mathbf{H}$ matrices (see Eq. (30)) were pre-calculated rather than looping the calculation for each harmonic.

Figs. 9–11 also show stability boundaries predicted using the well-established time domain numerical integration method and the semi-discretization method. For the case of the numerical integration scheme, the time step was kept at 2.6×10^{-4} seconds for predictions for the case of workpiece-flexure being flexible, and 6.6×10^{-5} seconds for predictions for the case of the tool being flexible. And, for the case of the semi-discretization method, the number of points per period of the highest natural frequency oscillation wave was selected to be at least six, i.e., three times that required by the Nyquist sampling theorem. For predictions for the case of the workpiece-flexure being flexible, each period (revolution) was discretized in 20 steps, and for the case of the tool being flexible, each period was discretized in 60 steps. Number of steps was calculated at the lowest simulated spindle speed (i.e., 4000 rpm).

For both time-domain methods, and for the Nyquist check for the ZOA and the MFS methods, the increments in the depths of cut were taken to be 0.02 mm, and the spindle speed increment was set as 40 rpm, making for a simulation grid of 50×200 points for predictions for the case of the setup in which the workpiece-flexure system is flexible. For predictions for the case of the setup with the tool being more flexible, the increments in the depths of cut were taken to be 0.16 mm, and the spindle speed increment was set as 60 rpm, making for a simulation grid of 50×100 points. The increments and grid space were selected to accurately characterize the stability behavior.

Experimental observations are overlaid over model predictions in Figs. 9–11 for all three cutters of interest. As is evident, for all cutters, model predictions using the five different methods, in general, agree with each other, and with experimental observations, except for the prediction with the graphical method for the trapezoidal cutter shown in Fig. 11. If the time domain numerical integration scheme is considered the gold standard, then the SDM compares equally well with it, and as does the MFS method. In general, the stability predictions with time

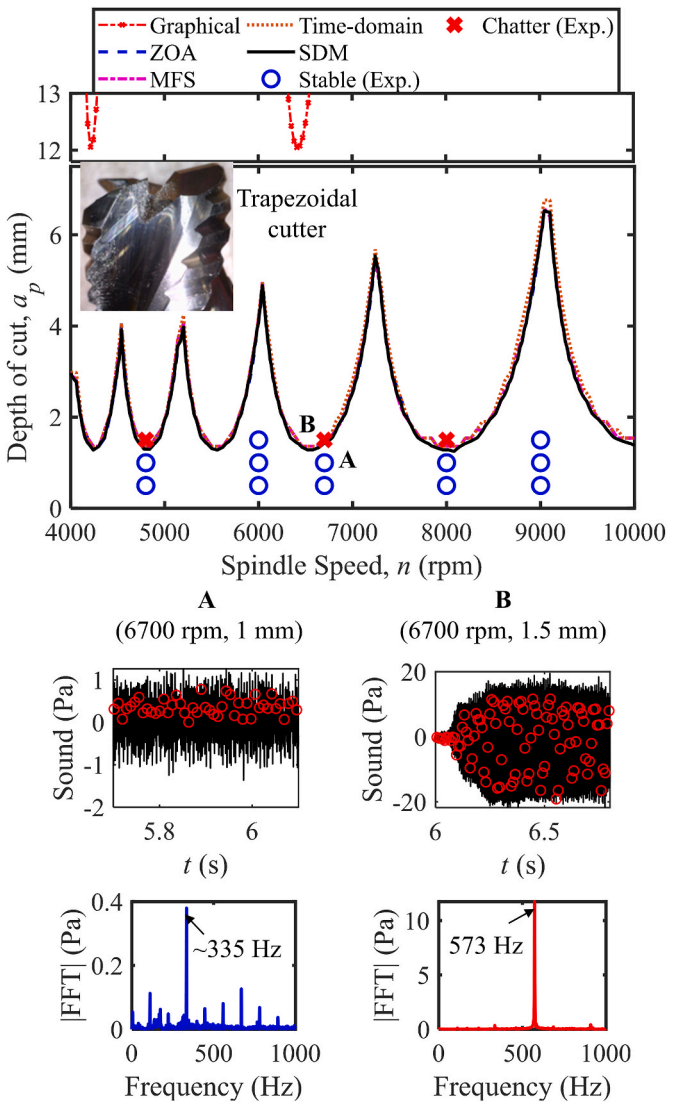

Fig. 11. Stability behavior for the standard profiled trapezoidal serrated cutter with uniform pitch and helix for slot cutting with 0.05 mm/tooth/rev feed rate. Time history for measured microphone sound signal is overlaid with once-per-revolution sampled data ('o' symbol). Experiments were conducted on the setup shown in Fig. 6(b).

Table 2
Summary of computational efforts to generate stability boundaries using different methods.

Stability models	Inclined circular serrated cutter	Semi-elliptical serrated cutter	Trapezoidal serrated cutter
Graphical method	6 s	8 s	6 s
ZOA	26 s	27 s	44 s
MFS	5.8 min	5.7 min	8.6 min
Time-domain	2.1 h	2.5 h	1.6 h
SDM	16 min	16 min	41 min

domain methods and the MFS method are more accurate because of the approximations that ZOA and graphical methods involve to obtain time invariant equations.

Though less accurate, the graphical methods are computationally much more efficient at generating stability boundaries shown in Figs. 9–11 than any of the other four methods. For the cutters of interest, the graphical methods take ~5–6 s to generate stability boundaries in contrast to the ZOA method that takes ~26–44 s, or the MFS method that takes ~5–9 min, or the SDM method that takes ~16–41 min or the time-domain numerical integration scheme that takes ~1.6–2 h or more. Significant improvements are achieved over reports in the previous literature. The graphical method reduces the simulation time by up to ~99% compared to the semi-discretization method. And the use of the zero-order approximation method and the multi-frequency method reduces simulation times by up to ~97% and ~79% respectively compared to the semi-discretization method. All computer programs[1] were executed in MATLAB® 2018a and implemented on a computer with specifications of: Intel Core (TM) i7 Processor, 3.6 GHz, 16 GB RAM. A summary of the computational effort to generate stability boundaries is presented in Table 2.

Furthermore, even though less accurate, the graphical and ZOA methods effectively capture the low- and the high-speed (4000–7000 rpm and 9000–12000 rpm) stability behaviour for both the non-standard profiled serrated cutters, results for which are shown in Figs. 9 and 10. However, due to their approximate nature, both these methods cannot capture the period-doubling (flip bifurcation) that results in a narrow lens around the 8500–9000 rpm range. For regular tools, the period-doubling behaviour is usually associated with low immersion cutting rather than slot cutting (i.e., 100% immersion) used in the experiments. However, interrupted cutting with serrated end mills inherently causes multiple delays and 'missed-cut' effect for any immersion condition. Hence the occurrence of these flip lobes is not unexpected for serrated tools [4]. The jaggedness of the stability boundaries evident in Figs. 9 and 10 is due to the coarse sized grid used in ZOA, MFS, and both time domain methods. Smoother boundaries would result from a finer sized grid at considerable additional computation expense.

The dynamic flexure used was much more flexible compared to both cutters used in the experiments. So, as seen in Figs. 9 and 10, the spindle speed-dependent trends of the stability boundaries are the same for both tests due to the flexure's natural frequency affecting the chatter frequency. On the other hand, the limit depths of cut are not the same for the different cutters. This is expected due to the different serration profiles of the tools, and since one tool has a non-uniform tooth spacing and the other has not. Hence, a direct comparison between the stability of these cutters is not advised and is also not intended.

Since the speed-dependent stability behaviour for both the non-standard profiled serrated cutters is similar, experiments for both were conducted at speeds of 4770 rpm, 6000 rpm, 8730 rpm, and at 11000 rpm – see data points overlaid in Figs. 9 and 10. Of these, experiments at 4770 rpm and at 8730 rpm were conducted to test the boundaries, and experiments at 6000 rpm and 11000 rpm were conducted to test the presence of stability pockets. As is evident from results in Figs. 9 and 10, cutting at points that lie above the boundary and within the lens are characterized by the FFT spectra being dominated by a peak at 217–218 Hz, i.e., just above the natural frequency of the flexure. For cutting at points that are stable and within the pockets, the FFT spectra display peaks at ~100 Hz and at ~183 Hz, i.e., corresponding to the spindle speeds of 6000 rpm and 11000 rpm, respectively. Since the nature of the process is intermittent due to the 'missed-cut' effect, the FFT spectra for the stable case are dominated by the spindle rotation frequency harmonics rather than the tooth-passing frequency harmonics. For cutting at regions below the lobes and lenses, the response spectra show frequency content at the tooth passing frequencies as well as at frequencies (with relatively lower peak) just higher than the natural frequencies – suggesting that these are indeed transition regions.

For the case of the standard trapezoidal profiled serrated cutter, results for which are shown in Fig. 11, the stability boundaries are different and occur at higher depths of cuts than the stability for the non-standard profiled cutters. Differences are mainly due to the dynamics for

[1] MATLAB codes for all methods are supplied as supplementary data.

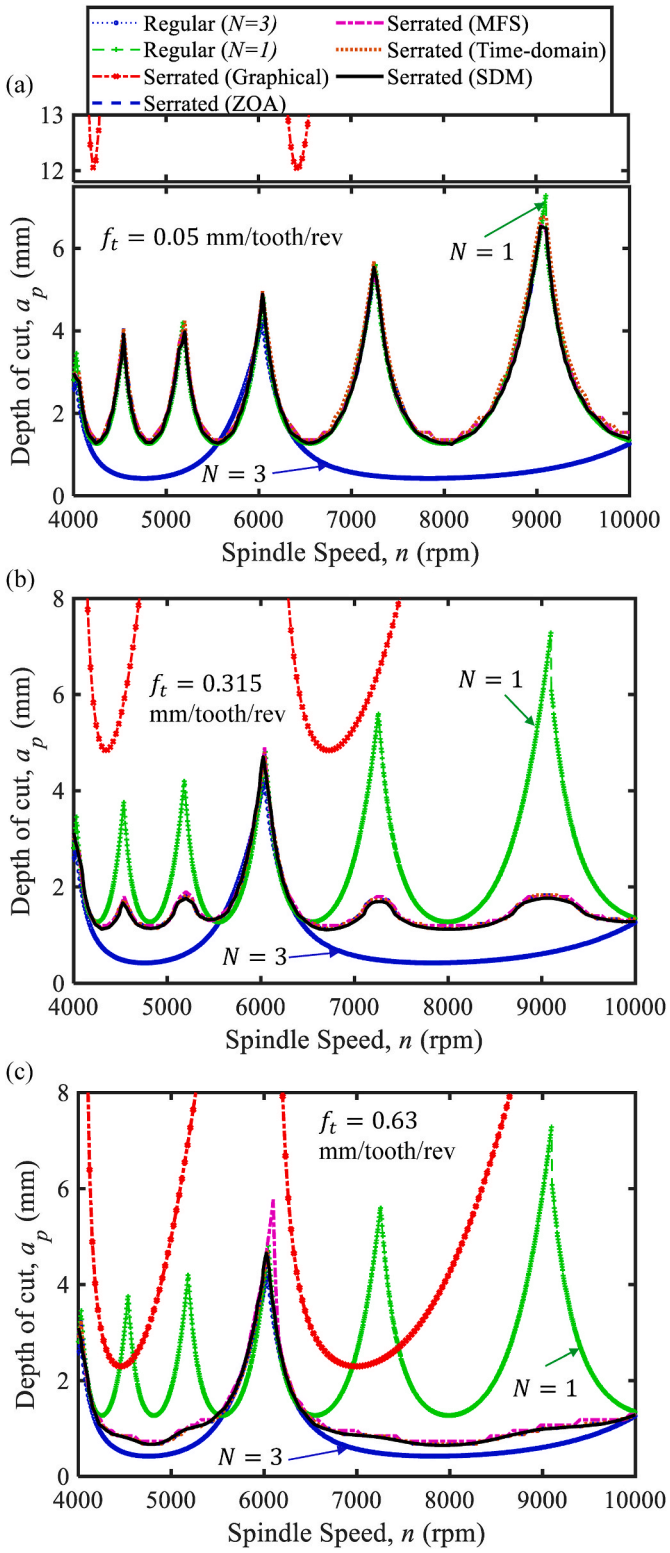

Fig. 12. Influence of feed on the stability for a three-fluted trapezoidal serrated cutter with uniform helix and pitch using five solution methods - graphical, ZOA, MFS, time-domain, and SDM. Cutting conditions: slot cutting with three levels of feed rates: (a) 0.05 mm/tooth/rev (b) 0.315 mm/tooth/rev and (c) 0.63 mm/tooth/rev.

this case being dominated by the tool's modes in its *x* and *y* directions and not the workpiece-flexure mode as was the case for the non-standard serrated cutters. Results demonstrate that the ZOA and the MFS methods are as accurate as the SDM and the time-domain methods. On the other hand, the graphical method fails to correctly predict these boundaries. Since the modes are closely spaced (close in frequencies) with similar relative flexibilities in each of the *x* and *y* directions, the magnitude of oriented FRF becomes almost equal to zero. Hence the stability limit in the graphical method becomes unrealistically high because of being inversely proportional to the real part of FRF. This is an inherent limitation of the graphical method.

Experiments to validate predicted stability for the case of cutting with the standard trapezoidal profiled serrated cutter were conducted at five different spindle speeds as shown in Fig. 11. Representative measured sound signals and their spectra for cutting at depths of cuts of 1 mm and 1.5 mm at a spindle speed of 6700 rpm are shown in Fig. 11. As is evident, for a cut at parameters below the predicted boundary (1 mm, 6700 rpm), the spectrum of the recorded sound is dominated by a peak at ~335 Hz that corresponds to the tooth passing frequency. For cutting at a depth of cut of 1.5 mm that lies near the predicted boundary, the recorded sound exhibits classic finite amplitude chatter vibration characteristics [12], and the spectrum of the recorded sound is dominated by a peak at ~573 Hz. Interestingly this frequency does not correspond to the spindle frequency or the tooth passing frequency and/or any of its harmonics, and nor does it appear near the natural frequency of the tool which is around ~604 Hz. Though unusual, chatter frequencies in milling can occur below the tool's frequencies, as has been reported in Ref. [40]. Moreover, the once-per-revolution sampled data for this case clearly shows a quasiperiodic behaviour – which is a characteristic of the Hopf bifurcation [18], confirming that this is a chatter condition. On the other hand, the once-per-revolution sampled data for cutting at 1 mm at the same speed approximates a straight line suggesting that the cut is stable, as is indeed confirmed by the frequency spectra. The predicted behavior is hence deemed validated.

The validated stability charts presented in Figs. 9–11 were for a single feed rate setting. Since feed influences stability, we further simulated the influence of feed rate in Fig. 12. Results in Fig. 12 are presented for the representative case of the standard trapezoidal profiled cutter being flexible in both its *x* and *y* directions. Three levels of feed rate are considered. The first case, shown in Fig. 12(a) corresponds to the feed rate of 0.05 mm/rev/tooth. The second case, results of which are shown in Fig. 12(b) corresponds to the feed rate being half the serration amplitude, i.e., 0.315 mm/tooth/rev. The third case shown in Fig. 12(c) corresponds to the feed rate equalling the serration amplitude, i.e., 0.63 mm/tooth/rev. Stability is predicted with all five methods, i.e., the graphical, the ZOA, the MFS, and the SDM and the time-domain methods. Stability behavior for each of the cases is also compared with equivalent three and one fluted regular end mills, stability for which is obtained using the ZOA method.

As is evident from Fig. 12, results for three levels of feed show that when the ratio of the feed per tooth to the amplitude of serration amplitude is small, the stability behaviour of a three-fluted serrated cutter approximates that of an equivalent one-fluted regular end mill. When the feed is of the order of the serration amplitude, the serrated cutter loses its advantage over an equivalent three-fluted regular end mill. This observed behaviour is in line with reports in Refs. [4,23]. Capturing this behaviour further validated the efficacies of our proposed models (except for the graphical method which fails due to the closely-spaced vibration modes).

Though our newly proposed solution schemes are validated, proposed methods, especially the graphical one, do have limitations. An overview of these and of the advantages our proposed methods offer is summarized next.

5. Discussions, limitations, and advantages

It has been shown that the graphical method has superior computational ease and efficiency when compared to other numerical techniques. The graphical method averages out the time varying effects of the milling process. So, ideally, the stability limit from graphical method should be close to the one obtained from ZOA method. However, like Tlusty's average tooth angle approach [13], the graphical method has limitations that can be understood for cutting with a system that has a vibration mode in each of the x and y directions:

- For closely-spaced modes with similar relative flexibilities in each of the x and y directions, i.e., as with the case for the setup shown in Fig. 6(b), stability results were shown in Figs. 11 and 12. Since the magnitude of oriented FRF becomes almost equal to zero, the stability limit in the graphical method becomes unrealistically high because of being inversely proportional to the real part of FRF.
- For the case of the x and y directional modes being widely spaced and having similar relative flexibilities, the graphical method works better than when the modes are close, and this is true for all immersion conditions.
- However, if slot cutting is assumed along the x direction, and if the y directional mode is a lot more flexible than the x, since the chip displacements and modes are projected along the x direction for slotting (recall Fig. 2), the y directional mode(s) will have no influence on the oriented FRF, and, as such, again, unrealistically high stability limits will be obtained. However, with immersion conditions other than slotting, the graphical method will work with reasonable accuracies for cutting along the x direction for when the y direction is more flexible.
- If, on the other hand, the x direction is flexible and y direction is rigid – as it is in the experimental setup shown in Fig. 6(a), the graphical method will work with reasonable accuracy at all radial immersion conditions.

The ZOA method gives accurate results for the cases where the graphical method has limitations. This is due to keeping the eigenvalue problem of the two-dimensional case similar to the [22]. The coupling of the directional factors in both directions is preserved. The ZOA is accurate because of considering the average dynamic forces that are mainly responsible for the milling chatter. Computation of ZOA becomes very fast with the use of Nyquist criterion, hence it is a good alternative to cover the limitations of the graphical methods. Furthermore, in contrast to other contemporary work [24] which also averaged the delay and solved the resulting characteristic equation using the Nyquist stability criterion, but suffered from accuracy issues, our implementation of the ZOA method, as is evident from comparisons in Figs. 9–12 is accurate and fast.

Serrated tools inherently show highly interrupted cutting behavior, independent of radial immersion, which results in multiples of spindle rotation frequency affecting the cutting forces. Although ZOA gives close predictions through most of the stability diagram, it fails to capture the frequency modulations around the chatter frequency. The MFS method can capture the high frequency effects in the time-varying directional factors as good as the semi-discretization method. In the previous literature, the MFS needed high computational load [38] due to the iterations involved, so not much attention was given to apply it for end mills with non-uniform geometry. It has been shown for the serrated tools that the ZOA formulation can be extended to MFS. Moreover, the additional use of Nyquist criterion to search for the chatter frequency eliminates the need of iterations. For the case with one dominant vibration mode and/or for the case of two flexible and closely spaced modes discussed in this paper, the MFS method was faster than the SDM. However, if the number of vibration modes increases and if those modes are not closely spaced, the required search range for frequencies will also increase and the MFS method may take longer than the SDM.

Semi-discretization method, a well-established time-domain method for estimating stability boundaries, is used for verification. The time-varying directional factors are considered at each time step. Unlike the frequency domain methods accepting "as-measured" frequency response functions (FRF), time-domain methods need modal parameters which are obtained by curve fitting. Recent research by Ref. [37] aims for using the "as-measured" FRFs directly. Another limitation of time-domain methods is that the time step size needs to be smaller at lower spindle speeds. This may result in needing very high computational load due to the larger size of transition matrix, which is not a concern for the frequency domain methods.

6. Conclusions and outlook

Serrated end mills are widely used due to their superior stability characteristics and high-productivity machining capability of difficult-to-cut materials. Designing such tools is complex because the serration geometry has infinite design possibilities to achieve optimal stability for a given cutting condition. Moreover, the process involves interrupted cutting action which makes the tool performance dependent on the feed rate. With the state-of-art numerical methods, the simulation times are prohibitively long which would keep the tool designers away from using them in optimizing the tool geometry. This paper responds to the need of a fast and reliable simulation approach and brings a new understanding to the engineering design of serrated tools and other tools with non-uniform geometry.

Novel methods for simulating the chatter stability diagram of serrated tools are presented, and they are further validated by experiments and time domain simulations: Two fast methods, graphical and zero-order approximation methods, are developed to calculate stability diagram of serrated end mill with any serration profile and pitch/helix angles. The methods are experimentally validated for various tool geometries. The multi-harmonic frequency domain method is derived to calculate the stability diagram. It is shown that the instability due to flip bifurcation can be simulated accurately, the results match well with the semi-discretization method.

The proposed methods are benchmarked with time-domain methods and the computational efficiency was analyzed. The graphical method can simulate very fast, and the ZOA method has reasonable simulation time and it can be preferred to cover the limitations of the graphical method. Though the graphical and ZOA methods are approximate, and in some known cases, less accurate, their ability to rapidly evaluate stability for complex profiled serrated end mills can be leveraged in the design optimization of serrated geometries to maximize stable cutting conditions – making the methods valuable for the manufacturing community. And, given that our use of the Nyquist stability criterion with the multi-frequency solution method is accurate and is more computationally efficient than the semi-discretization method, if higher fidelity predictions are desired, the multi-frequency solution can be thought of as an alternative to the use of the semi-discretization method. There are rooms for improvement, such as adaptive frequency stepping and numerical calculation of the integral equation, to further surpass the simulation times of the multi-frequency solution.

The proposed methods will form the base of our future work on rapid simulation of tools with non-uniform geometries. Our models will help instruct tool designers to make improved high-performance serrated and other end mills.

Credit author statement

Pritam Bari: Conceptualization; Formal analysis; Investigation; Methodology; Software; Data curation; Validation; Visualisation; Writing – original draft; Writing – review & editing. **Zekai Murat Kilic:** Conceptualization; Supervision; Investigation; Methodology; Visualisation; Writing – review & editing. **Mohit Law:** Conceptualization; Supervision; Funding acquisition; Validation; Visualisation; Project

administration; Resources; Writing – review & editing. **Pankaj Wahi:** Conceptualization; Supervision; review.

Declaration of competing interest

The authors declare that they have no known competing financial interests or personal relationships that could have appeared to influence the work reported in this paper.

Acknowledgements

The first author is grateful to the Shastri Indo-Canadian Institute for supporting his summer 2019 research stay at the Manufacturing Automation Lab at the University of British Columbia. The authors further acknowledge partial support for experiments made possible by the Government of India's Impacting Research Innovation and Technology initiative through project number IMPRINT 5509.

Appendix A. Supplementary data

Supplementary data to this article can be found online at https://doi.org/10.1016/j.ijmachtools.2021.103805.

References

[1] J. Tlusty, F. Ismail, W. Zaton, Use of special milling cutters against chatter, in: Proceedings of the NAMRC11, University of Wisconsin, SME, 1983, pp. 408–415.
[2] S.D. Merdol, Y. Altintas, Mechanics and dynamics of serrated cylindrical and tapered end mills, J. Manuf. Sci. Eng. 126 (2) (2004) 317.
[3] J.J.J. Wang, C.S. Yang, Angle and frequency domain force models for a roughing end mill with a sinusoidal edge profile, Int. J. Mach. Tool Manufact. 43 (14) (2003) 1509–1520.
[4] Z. Dombovari, Y. Altintas, G. Stepan, The effect of serration on mechanics and stability of milling cutters, Int. J. Mach. Tool Manufact. 50 (6) (2010) 511–520.
[5] B. Stone, Chatter and Machine Tools, Springer Cham Heidelberg, New York Dordrecht London, 2014.
[6] J. Burek, L. Zylka, M. Plodzien, M. Gdula, P. Sulkowicz, The influence of the cutting edge shape on high performance cutting, Aircraft Eng. Aero. Technol. 90 (1) (2018) 134–145.
[7] F. Tehranizadeh, R. Koca, E. Budak, Investigating effects of serration geometry on milling forces and chatter stability for their optimal selection, Int. J. Mach. Tool Manufact. 144 (2019).
[8] P. Bari, M. Law, P. Wahi, Improved chip thickness model for serrated end milling, CIRP J. Manufact. Sci. Technol. 25 (2019) 36–49.
[9] P. Bari, M. Law, P. Wahi, Geometric models of non-standard serrated end mills, Int. J. Adv. Manuf. Technol. 111 (2020) 3319–3342.
[10] R. Grabowski, B. Denkena, J. Kohler, Prediction of process forces and stability of end mills with complex geometries, Procedia CIRP 14 (2014) 119–124.
[11] B. Hosseini, A. Moetakef-Imani, H.A. Kishawy, Mechanistic modelling for cutting with serrated end mills – a parametric representation approach, Proc. IME B J. Eng. Manufact. 225 (2010) 1019–1032.
[12] J. Tlusty, F. Ismail, Basic non-linearity in machining chatter, CIRP Ann. 30 (1981) 229–304.
[13] J. Tlusty, W. Zaton, F. Ismail, Stability lobes in milling, Ann. CIRP 32 (1) (1983) 309–313.
[14] K.S. Smith, J. Tlusty, An overview of modeling and simulation of the milling process, ASME J. Eng. Indust. 113 (2) (1991) 169–175.
[15] R. Koca, E. Budak, Optimization of serrated end mills for reduced cutting energy and higher stability, Procedia CIRP 8 (2013) 570–575.
[16] Z.M. Kilic, Y. Altintas, Generalized mechanics and dynamics of metal cutting operations for unified simulations, Int. J. Mach. Tool Manufact. 104 (2016) 1–13.
[17] F. Tehranizadeh, E. Budak, Design of serrated end mills for improved productivity, Procedia CIRP 58 (2017) 493–498.
[18] T. No, M. Gomez, R. Copenhaver, J.U. Perez, C. Tyler, T.L. Schmitz, Force and stability modeling for non-standard edge geometry end mills, J. Manuf. Sci. Eng. (2019).
[19] P. Bari, M. Law, P. Wahi, Comparative analysis of cutting forces and stability of standard and non-standard profiled serrated end mills, 9th CIRP Conference on High-Performance Cutting, Procedia CIRP 101 (2021) 114–117.
[20] T. Insperger, G. Stepan, Semi-Discretization for Time-Delay Systems: Stability and Engineering Applications, Springer, New York, 2011.
[21] Y. Ding, L. Zhu, X. Zhang, H. Ding, A full-discretization method for prediction of milling stability, Int. J. Mach. Tool Manufact. 50 (5) (2010) 502–509.
[22] Y. Altintas, E. Budak, Analytical prediction of stability lobes in milling, Ann. CIRP 44 (1) (1995) 357–362.
[23] M.L. Campomanes, Kinematics and Dynamics of Milling with Roughing Tools, Metal Cutting and High-Speed Machining, Kluwer Academic Publishers, Plenum Press, Dordrecht, New York, 2002, pp. 129–140.
[24] N.D. Farahani, Y. Altintas, Chatter stability of serrated milling tools in frequency domain, J. Manuf. Sci. Eng. 144 (3) (2021), 031013.
[25] Y. Altıntas, S. Engin, E. Budak, Analytical stability prediction and design of variable pitch cutters, J. Manuf. Sci. Eng. 121 (173) (1999).
[26] S. Turner, D. Merdol, Y. Altintas, K. Ridgway, Modelling of the stability of variable helix end mills, Int. J. Mach. Tool Manufact. 47 (9) (2007) 1410–1416.
[27] N.D. Sims, Fast chatter stability prediction for variable helix milling tools, Proc. IME C J. Mech. Eng. Sci. 230 (1) (2016) 133–144.
[28] J.B. Niu, Y. Ding, L.M. Zhu, H. Ding, Mechanics and multi-regenerative stability of variable pitch and variable helix milling tools considering runout, Int. J. Mach. Tool Manufact. 123 (2017) 129–145.
[29] G. Totis, T. Insperger, M. Sortino, G. Stépán, Symmetry breaking in milling dynamics, Int. J. Mach. Tool Manufact. 139 (2019) 37–59.
[30] S.D. Merdol, Y. Altintas, Multi-frequency solution of chatter stability for low immersion milling, J. Manuf. Sci. Eng. 126 (3) (2004) 459–466.
[31] D. Bachrathy, G. Stepan, Improved prediction of stability lobes with extended multi frequency solution, CIRP Ann. - Manuf. Technol. 62 (1) (2013) 411–414.
[32] A. Otto, S. Rauh, S. Ihlenfeldt, G. Radons, Stability of milling with non-uniform pitch and variable helix Tools, Int. J. Adv. Manuf. Technol. 89 (9–12) (2017) 2613–2625.
[33] J. P Gurney, S.A. Tobias, A graphical method for the determination of the dynamic stability of machine tools, Int. J. Mach. Tool Des. Res. 1 (1961) 148–156.
[34] H.E. Merrit, Theory of self-excited machine-tool chatter, J. Eng. Indust. 87 (4) (1965) 447–454.
[35] M. Eynian, Y. Altintas, Analytical chatter stability of milling with rotating cutter dynamics at process damping speeds, J. Manuf. Sci. Eng. 132 (2) (2010), 021012.
[36] Y. Mohammadi, K. Ahmadi, Frequency domain analysis of regenerative chatter in machine tools with Linear Time Periodic dynamics, Mech. Syst. Signal Process. 120 (2019) 378–391.
[37] Z. Dombovari, Stability properties of regenerative cutting processes, based on impulse response functions expressed in the impulse dynamic subspace, Int. J. Mach. Tool Manufact. 162 (2021) 103691.
[38] Y. Altintas, Manufacturing Automation: Metal Cutting Mechanics, Machine Tool Vibrations, and CNC Design, Cambridge University Press, 2012, p. 54.
[39] L. Urena, E. Ozturk, N. Sims, Convergence analysis of the multi-frequency approach around a variable-helix instability island, Procedia CIRP 82 (2019) 279–284.
[40] T. Insperger, G. Stepan, P. Bayly, B. Mann, Multiple chatter frequencies in milling processes, J. Sound Vib. 262 (2) (2003) 333–345.
[41] CUTPRO V11.2, Advanced Machining Simulation Software ©MAL Inc.